Construction of the HUSIR Antenna

Nikolas T. Waggener

To add W-band capability to the Haystack X-band radar system, its 120-foot-diameter antenna was replaced with a new Cassegrain antenna with a surface tolerance of less than 100 μm. The installation of this antenna and its support systems was an incredibly challenging engineering construction project.

The original Haystack antenna, completed in late 1964, represented the cutting edge of antenna technology at the time. The antenna was built inside a 150-foot spherical radome, originally designed for use in extreme arctic environments and capable of withstanding 130 mph winds (Figures 1 and 2). Designed as a dual-use system, the antenna supported an X-band (~10 GHz) radar and radio-astronomy receivers at even higher frequencies. The 120-foot primary reflector was aligned to a surface accuracy of 1000 μm root mean square (rms) under worst-case thermal conditions [1]. A hydrostatic bearing in the azimuth axis effectively floated the entire rotating structure on a thin film of oil, virtually eliminating friction and resulting in exceptionally precise pointing and tracking capabilities.

Over the years, upgrades to expand Haystack's range of operational frequencies beyond the original 10 GHz included a water-based temperature control system for the primary reflector and, in 1993, a deformable secondary reflector that compensated for some of the surface error of the primary reflector and that yielded an equivalent surface accuracy down to 0.008 inches (200 μm) under certain conditions. However, these upgrades did not result in a system that could support the requirements of a wideband imaging radar at W band (~96 GHz), a capability seen as the next major technological step for imaging radars.

In 2002, when the planning for a new W-band radar began in earnest, one of the first considerations was whether to build a new system or transform the existing Haystack radar. On the basis of cost estimates from

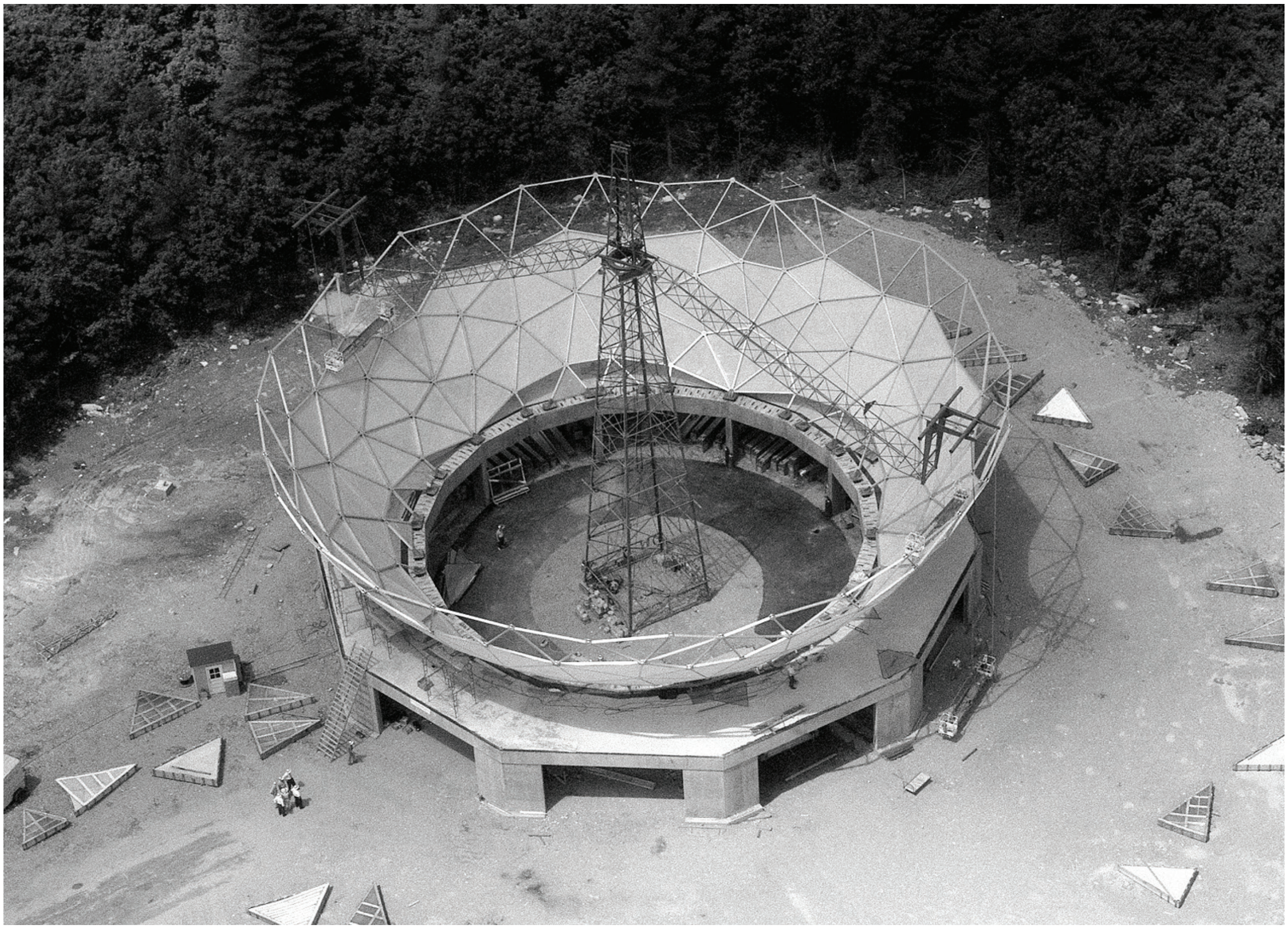

FIGURE 1. Construction of the Haystack radome in summer 1961 utilized a central derrick to support two diametrically opposed booms from which large aerial platforms were suspended.

FIGURE 2. Mobile cranes and extensive scaffolding were used to build the original Haystack antenna within the confines of the radome.

contractors, the project team decided to pursue a design that would leverage much of the existing Haystack facility (radome, infrastructure, site, hydrostatic azimuth bearing, and yoke) and to replace or supplement those components not compatible with the new higher-frequency capabilities (e.g., primary and secondary reflectors, waveguide pathway, and radio-frequency [RF] box). The resulting design and construction process lasted more than 10 years and drew on the efforts of many Lincoln Laboratory employees and outside organizations. A brief history of the mechanical integration of the new antenna is chronicled in this article.

Initial Work

In consultation with a number of subcontractors, most notably Simpson Gumpertz & Heger Inc. of Waltham,

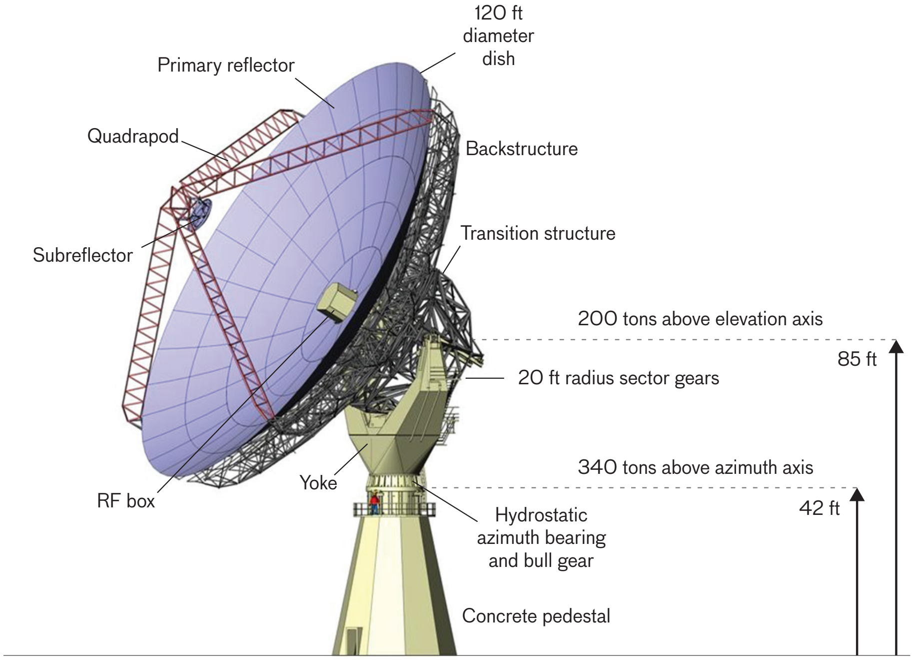

FIGURE 3. A computer-aided design rendering of the HUSIR antenna shows its key features.

Massachusetts, the engineering team considered various design options, including actively controlled positioners for the primary surface panels, before settling on the final strategy. The details of the final design* of the antenna are included in the appendix to this article. The heart of the upgraded antenna would be a stiffness-optimized primary reflector (backstructure). The backstructure was designed to deform such that it remains a paraboloid under gravity or temperature-induced loading, albeit with a different focal length that can be corrected by adjusting the position of the secondary reflector (subreflector). The rest of the new antenna structure was developed to support the optimized backstructure, while utilizing as much of the existing structure as possible (Figure 3).

By 2007, most of the design work was completed and fabrication of many subassemblies had begun. Working directly with subcontractors, the Lincoln Laboratory team oversaw the completion of the new antenna hardware. In 2008, construction began of the onsite facilities that would be used to perform the final assembly and integration of the various subassemblies, many of which would be too large to ship to the site fully assembled. The largest of these site projects was the construction of a 140 × 160 × 65–foot temporary fabric and steel building that would become the assembly area for the new backstructure, permitting work to proceed year-round and providing the controlled environment necessary for the aluminum welding work. Several smaller site improvements included assembly areas for the quadrapod (the support structure for the subreflector) and the transition structure (the steel backup structure that includes the elevation counterweights, drive gears, and bearings).

To minimize the impact of adverse weather during the critical lifts of the major subassemblies, the engineering team targeted spring 2010 for the start of the integration period. Because of the scope of the work and the relative inexperience of Lincoln Laboratory with large construction projects, the construction management firm Bond Brothers of Everett, Massachusetts, was hired to supervise daily operations at the site. Bond has a background in coordinating large civil engineering projects and a familiarity with the various skilled trades required to successfully complete this type of project. Keystone Engineering, formerly of Georgetown, Massachusetts, was contracted to provide much of the labor and equipment for the construction, and assembled a crew of highly skilled workers, primarily from the Local 7 ironworkers union. Hallamore Corporation of Holbrook, Massachusetts, supplied the 400-foot-tall Manitowoc 18000 MAX-ER crawler crane, which handled the

---

*The design of the antenna was originally proposed by Apostle Cardiasmenos of L-3 Communications ESSCO.

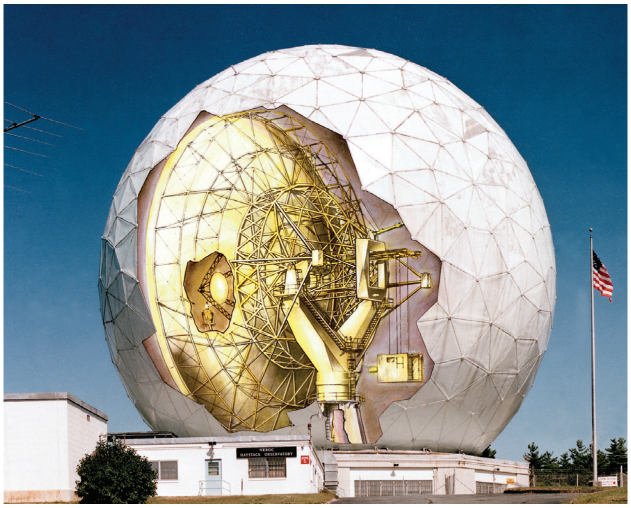

FIGURE 4. This rendering is a cutaway view of the old Haystack antenna that shows the RF box being lowered.

majority of the lifts during the integration phase, and several smaller truck cranes for ancillary lifts.

With all the subassemblies complete or on schedule, the logistics of the intricate integration phase planned out, and a complete team of Lincoln Laboratory personnel and subcontractors on board, the stage was set for the upgrade of the Haystack antenna into the Haystack Ultrawideband Satellite Imaging Radar (HUSIR).

RF Box Removal, April 2010

Onsite integration of HUSIR began with the removal of the old RF box, an 8 × 8 × 12–foot enclosure located at the Cassegrain focus of the dish, that contained the feed horn and associated transmit and receive (TX/RX) electronics for the X-band radar system. It was retracted through the rear of the antenna and lowered to the ground via a purpose-built overhead hoist system integrated into the antenna (Figure 4). At a nearby maintenance building, the RF box was modified to accommodate the addition of an 8 × 8 × 8–foot octagonal enclosure (Octagon), bolted to the front of the RF box, that provided space for the W-band TX/RX equipment, the support electronics, and a number of radio-astronomy receivers (K, Q, and W band) (Figure 5).

The Haystack antenna had long supported both radio-astronomy and radar operations, but transitioning between these operations had required swapping the electronics box. Combining the radar and radio-astronomy equipment into a common RF box enabled this laborious, time-consuming swap to be accomplished nearly instantaneously. The W- and X-band feeds would be located at the Cassegrain focus of the antenna, as the original X-band feed had been. The W-band path diverts just in front of the Octagon by means of a frequency-selective surface (FSS) positioned at a 45° angle with respect to

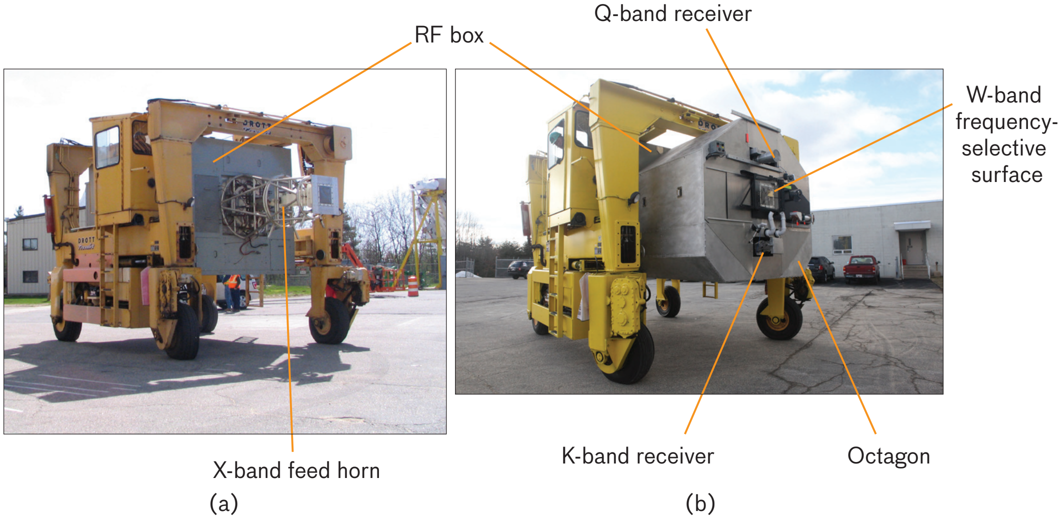

FIGURE 5. (a) The old RF box was transported to a temporary storage area for upgrading. The truss structure on the right supports the X-band feed horn. (b) The modified RF box is shown with the Octagon installed. The Octagon encloses the X-band feed horn while providing additional space for the new W-band hardware and radio-astronomy feeds.

the antenna boresight. The FSS, an 18 × 22–inch sheet of high-purity quartz with a 3.5 × 5–inch rectangle of gold tripoles set in the middle, permits X-band waves to pass through while diverting the W-band waves along an orthogonal path. The radio-astronomy feeds are offset from the Cassegrain focus (i.e., above and below) and are illuminated by repositioning the subreflector.

Old Antenna Disassembly, April–June 2010

Once the RF box was removed, the antenna was rotated to zenith; a crane was used to compensate for the imbalance resulting from the absence of the RF box (Figure 6). Then, the demolition of the old antenna surface and backup structure began.

The new antenna would reuse the major structure of the Haystack antenna from the ground to the elevation axis, but the surface tolerance required for W-band operations could not be met with the legacy primary surface or its support structure. Because the combined weight of the components to be removed exceeded the capacity of the large crane brought in for lifting them, it was necessary to separate the structure into smaller subassemblies. The surface of the primary reflector (a 5/8-inch-thick sandwich panel of aluminum sheet with a honeycomb core) was cut into small sections and removed one piece at a time (Figure 7). All connections between the surface and the backup structure were severed, except the four bolted connections that would remain intact until the day of the lift. The 30-ton, concrete-filled counterweight, temporarily supported on cribbing in the junction of the yoke, would be removed separately.

Meanwhile, the inside of the yoke and tower structures were gutted of all legacy equipment to make room for the updated hardware. The old hydraulic drive systems for both elevation and azimuth were replaced by modern electric motors that afford better control. Dozens of cables and hoses were replaced with new versions or with upgrades to newer technology; for example, some signal cables were switched to fiber-optic lines.

Because the original antenna had been designed for, and built within, the confines of the radome, no provisions for wind loading had been included in its design. The lack of wind protection would become a concern once the workers began removing the radome skins in preparation for uncapping the radome. Analysis indicated that at wind speeds as low as 55 mph the antenna could tip off the 14-foot-diam-

FIGURE 6. A crane connected to the 30-ton counterweight compensates for the missing RF box as the antenna is rotated to zenith for the last time.

(a)

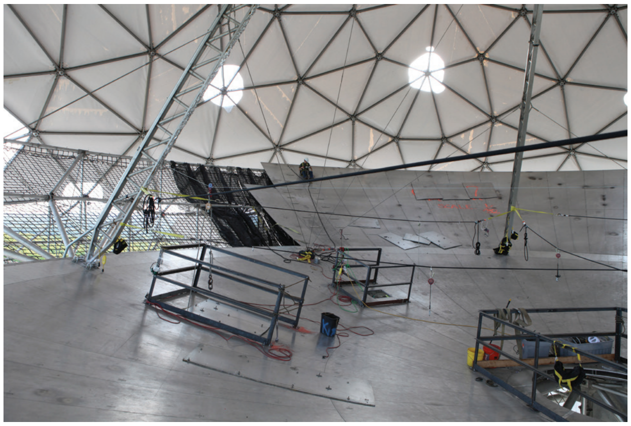

(b)

FIGURE 7. (a) Workers remove the first sections of the old antenna surface. (b) Meanwhile, radome membranes are dismantled around the separation line at which the radome will be "uncapped."

eter azimuth bearing. To resolve this problem, 20 custom C-clamps were built, each capable of applying 35 tons of force, and installed around the azimuth bearing to secure the rotating and stationary sections together (Figure 8).

Radome Cap Removal, May 2010

As work progressed inside, workers were also preparing the 150-foot radome structure for the removal, or uncapping, of its upper third. This uncapping would give the large crane access to the antenna structure for the removal and replacement of all the major subassemblies. The radome, a 1950s design, is a space-frame type in which the aluminum beam and node structure is self-supporting and the skins are non-load-bearing membranes that rely on the structure to maintain their shape. Unlike most contemporary radomes (in which each skin is both the enclosing surface and the support structure), this space-frame design permitted the removal and replacement of the membranes without a complete disassembly and reassembly of the entire structure. The material chosen for the new radome membranes minimizes signal loss at both X and W band; the old membranes had high loss coefficients around W band (see the section on radome recapping for more detail).

FIGURE 8. The 200 lb clamps around the azimuth bearing ensure that the antenna does not tip over when exposed to high winds.

Uncapping the top third of the radome required the removal of the membranes immediately above and below the split-line, the replacement of the nodes along the split-line, and the installation of a stiffening ring around the split-line. Wind-load analysis had shown that, although the intact radome can withstand 130 mph wind loads, without the cap such wind loading on the truncated radome would cause significant deflections and possibly damage the radome or the antenna within. Therefore, membranes were removed below the split-line to reduce

FIGURE 9. The ground support nodes in the foreground await the radome cap. In the background, the radome equator region is almost completely de-skinned, exposing the old Haystack antenna for the first time in its history.

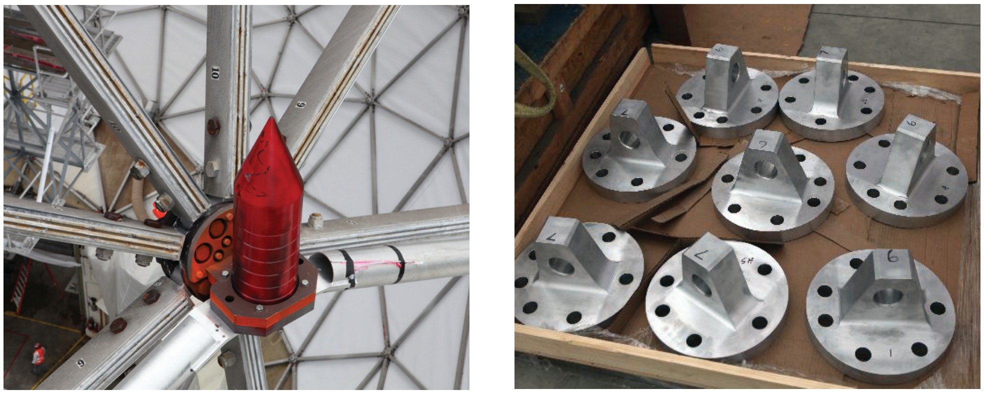

(a)

(b)

FIGURE 10. (a) Each split-line node has alignment cones and stiffening tubes that replicate the support of the beams that would be lifted with the cap. This cone was painted red to help index the position of the cap for reinstallation. (b) The lifting nodes in this box are ready for installation.

the wind-loaded area to an acceptable level. Figure 9 shows the radome during membrane removal. Like the radome nodes they replaced, the split-line nodes connect the radome beams where they intersect, but were specially designed to split to permit the radome cap to be lifted away. The split-line nodes were also built with provisions for installing a stiffening ring, which would help the truncated radome maintain its shape once the cap was removed.

A major concern in regard to the radome separation was the possibility that the node locations along the split-line would not realign when the cap was reinstalled. Three likely sources of deformation were identified:

1. Residual strain energy from the original construction could cause the structure to "spring" out of shape when the geometry was disturbed.
2. Deformation of the radome cap during the lift could result from the rigging loads or uneven tension in the lifting straps.
3. Deformation of the unsupported top edge of the truncated radome could occur.

The addition of the stiffening ring of tubes paralleling those beams that would be lifted with the cap was designed to mitigate risks 1 and 3. On the basis of a thorough finite element analysis of the structure, risk 2 was addressed with the rigging design and placement of the lifting nodes. These nodes had provisions for connecting lifting hardware, and their locations were selected to mimic the in situ loading configuration as closely as possible, resulting in the least deformation along the split-line. In addition to these precautions, the newly installed split-nodes were equipped with a cone-and-ring feature that would assist in matching the 35 node halves with their mates (Figure 10). The cone heights were staggered so that five of the alignment features would come into contact sequentially, progressively aligning all 35 nodes as the cap was lowered.

The removal of the radome cap was the first of several major crane operations involving the large Manitowoc 18000 MAX-ER crawler crane (Figure 11). The crane, one of only a handful in the United States at the time, stood almost 400 feet tall and weighed more than 2 million pounds. It was transported to the site on more than 50 tractor trailers, 35 of which were dedicated to counterweight blocks. Once at the site, the crane had to be assembled with the help of several smaller cranes (Figure 12). To prevent the high ground pressure under the crane crawlers from destabilizing the asphalt parking lot, a 100-foot-diameter "crane mat" of 12-inch-thick timber beams was laid down over the entire area on which the crane would be operating.

The radome cap, with its split-nodes, reinforcing ring, and lifting nodes installed, was scheduled to be lifted during the early morning hours of 26 May 2010. (To minimize wind loading, all major lifts during the HUSIR construction were planned for early morning hours when predicted wind speeds were the lowest.) However, when the weather turned blustery and thunderstorms rolled through the region, the lift was postponed. The following night the weather was clear and calm, and the first major lift of the HUSIR upgrade commenced (Figure 13). The 60-ton radome cap was lifted clear of the split-line, raised above the height of the antenna's secondary reflector, and slowly swung over

FIGURE 11. The assembly of the heavy-lift crane takes place along a 400 ft roadbed built into the treeline while the radome membranes around the equator are removed in preparation for the separation of the radome cap. The temporary landing zone for the cap is the ring of steel piers in the lower right corner.

FIGURE 12. The author stands behind the auxiliary counterweight cart while a smaller crane assists with assembling the crane.

FIGURE 13. The 400-foot-tall main crane and smaller support cranes are silhouetted against the sunrise just after the radome cap is lifted. Photograph by Colin Lonsdale.

the Haystack office building to the adjacent parking lot (Figure 14). Waiting in the parking lot were 35 steel columns anchored to the bedrock and laid out in the same configuration as the nodes along the split-line. Each column was topped with a duplicate split-node lower half and alignment cone, creating a replica of the split-line. The radome cap was lowered into place, and the cone-and-ring alignment features brought the two split-node halves together for a successful landing.

FIGURE 14. The cap was lifted off the Haystack radome and carefully swung to its temporary landing site.

Old Antenna Removal, June 2010

The newly exposed antenna dish was scheduled to be lifted out of the radome a week later and placed on cribbing in an adjacent parking lot to await demolition. As with all HUSIR lifts, the rigging design and crane capacity calculations included a substantial design factor beyond the built-in safety factors required by industry standards. Moreover, project policy was to halt any lift if the actual weight, as shown on the load indicator in the crane operator's console, exceeded the predicted load by more than 5%.

As the backstructure lift began, the crane operator alerted the engineers that the total weight was exceeding the 32-ton weight estimate that was based on information from the original construction documents. Workers located at the separation point on the top of the yoke confirmed that all fasteners were removed and that nothing appeared to be jammed. The team decided to increase the load limit to 38 tons, but this limit still proved insufficient.

The team concluded that the discrepancy between the weight estimate from the 1960s documentation and the actual weight was likely due to modifications that had been implemented since the original construction, including personnel access netting, a stiffer support ring for the surface panels, and a water-cooled distortion mitigation system.

The team authorized the crane operator to increase the load to the maximum allowable load of the weakest component: 43 tons. If the weight exceeded that limit, the lift would have to be postponed until the rigging plan could be modified. When the structure finally did lift free of the yoke, the weight of the backstructure was 35% more than originally anticipated and nearly 100% of the rated load of the weakest rigging component (Figures 15 and 16). The mystery of the antenna weight was com-

FIGURE 15. The 43-ton old backstructure was lifted over the edge of the radome and set down behind the temporary building to await demolition.

FIGURE 16. Under heavy loads, the crane's 230-ton auxiliary counterweight lifts completely off the ground.

pounded when the primary counterweight was removed a few days later; it weighed 15% less than expected.

Yoke Modifications, April–August 2010

Internal yoke modifications, primarily to the azimuth drive support area, had been ongoing since the start of the integration phase. The azimuth motors drive pinion gears against a 12-foot-diameter internally toothed stationary bull gear located between the steel yoke and the concrete pedestal. Because the bull gear is part of the azimuth bearing, and therefore inaccessible without removal of the yoke, this 50-year-old component would not be upgraded as part of the HUSIR project. To minimize the risk of fatigue failure caused by higher inertia and higher acceleration rates, the number of drive pinions in the upgraded antenna was doubled from four to eight, thereby reducing the individual tooth loads to an acceptable level. The additional drives would permit the antenna to reach its design speed of 5°/s and acceleration rate of $2°/s^2$.

The four new pinions, and their associated gearboxes and motors, had to be installed in the already crowded upper distribution ring (the bottom of the rotating yoke structure). To ensure proper seating and balanced tooth loading, the mounting surfaces for the new gearboxes had to be machined flat. In the confined space of the upper distribution ring, this task required workers to use a high-precision portable milling machine and to perform careful fixturing. Once machined, the four low-speed gearboxes (each gearbox houses two independent transmission paths leading to two pinions), each weighing a ton, had to be lowered in from above and positioned with a series of overhead hoists and lateral rails (Figure 17). The final alignment of the pinions to the bull gear required a parallelism between the teeth of less than 0.005 inches in both radial and circumferential directions and a backlash (free play between mating teeth) of approximately 0.015 inches (Figure 18). Because of the potential deformation of the mating surfaces, the final alignment could not be performed until the full weight of the new antenna was in place.

With the old backstructure removed, the scaffolding tower erected for convenient access to the outside of the yoke structure could be extended so that workers could cut off the tops of the yoke tips and install a new top plate approximately 6 inches below the old one (Figure 19). The new top plate was designed to accommodate the new, larger elevation bearings without having to modify the effective height of the elevation axis. Cover plates installed between the two separate yoke tines, where the old elevation sector gears had been located, stiffened the yoke tips for the increased load. The new sector gears located close to the center of the yoke notch have a 20-foot radius versus the 6-foot radius of the legacy gears (Figure 20). This increased moment arm reduces the loading on the gear teeth and the requirements of the elevation drive motors, which would be mounted on new, 2-inch-thick, support structures welded to the top and front faces of the yoke notch.

New Transition Structure Lift, August 2010

Once completed, the modified yoke was ready to receive the new transition structure. This steel structure carries the weight of the backstructure, provides the mounting points for the new sector gears, and houses the counterweight to balance the antenna about the elevation axis. Subassemblies of the steel transition structure were built at a local vendor's site before being transported to the Haystack site in June 2008. The majority of the structure was assembled in a face-down (sector gears facing up) orientation on a concrete pad near the Haystack radome. The assembly sequence included the precision alignment of the two 40-foot-long sector gears. Finite element models indicated that for the sector gears to sweep a circular arc through their 90° range of motion, they had to be installed with some built-in deviations from an arc (up to 0.075 inches) to compensate for the deformation of the transition structure as it rotated from face-side to face-up orientation. These intentional deviations from a circular

FIGURE 17. The first of the 1-ton gearboxes is lowered into the yoke. The gearbox was then transferred to a series of overhead chainfalls and a rail system in order to position it in place.

FIGURE 18. One of four pairs of pinions that drive against the stationary 12-foot-diameter bull gear. The shaft on the right is awaiting installation of the pinion gear.

FIGURE 19. Towers of scaffolding ascend from the floor of the radome as the yoke structure is stripped of old components and modified to accept the new transition structure.

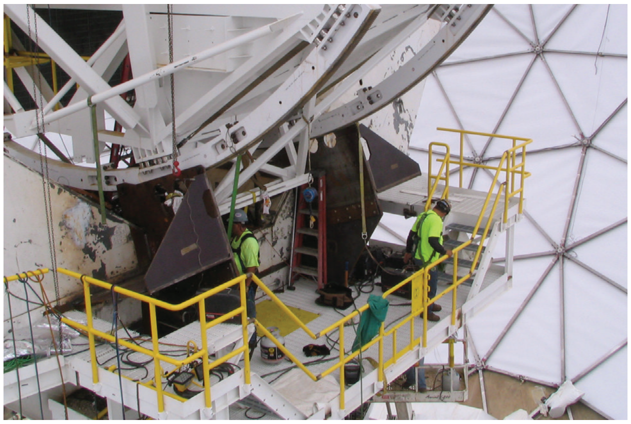

FIGURE 20. Workers install the 2-inch-thick steel plate assemblies that will become the new elevation drive mounting points. The elevation sector gears are just inboard of the mounts.

profile ensured uniform tooth contact and wear on the sector gears by keeping the nominal pitch line of the sector gears within ±0.008 inches.

The elevation axis rotates on a pair of precision tapered roller bearings contained within the bearing boxes on either side of the transition structure (Figure 21). A 6-foot-long "stub shaft" projects outward from each bearing box to interface with the mounting features (saddle assemblies) on the yoke tips. The inner and outer races of the bearings are permanently mated to the stub shaft and bearing box, respectively, by a thermal fit (i.e., liquid nitrogen is used to shrink the inner components prior to assembly, locking them in place once they return to room temperature) (Figure 22). This configuration of tapered roller bearings provides good load capacity and stiffness in the radial and axial directions, but does not transfer moment loads into the transition structure, thereby avoiding the possibility of such moment loads distorting the transition structure and degrading the shape of the new dish.

When the assembly of the transition structure had progressed as far as possible in the face-down configuration, the partially completed 66-ton assembly was moved to a pair of custom-built support stands and inverted through a tandem lift sequence utilizing two cranes (Figure 23). The support stands were sufficiently elevated to permit installation of the transition structure in the face-up orientation without damaging the exposed sector gear teeth (now

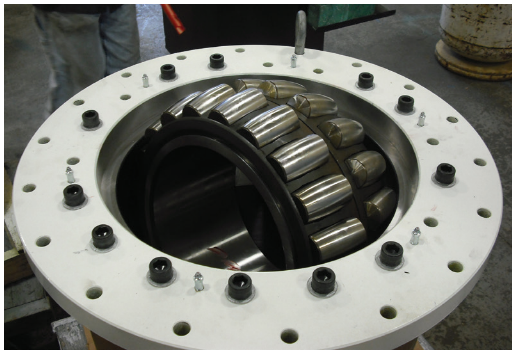

FIGURE 21. One of the elevation axis spherical roller bearings is assembled into its outer race.

FIGURE 22. Liquid nitrogen boils as the 6-foot-long stub shaft is lowered in. Once cooled, the stub shaft is pressed into the inner race for a permanent "thermal fit."

FIGURE 23. During a tandem lift operation, the transition structure is inverted and moved from its face-down assembly area to a pair of supporting tripods where final integration continues face up.

located a few feet off the ground). Then, the components that project beyond the plane of the elevation axis, primarily access platforms for the RF box and mounting points for the backstructure, were installed on the structure.

The 85-ton completed assembly, shown in Figure 24, was lifted and set into position on 100-ton hydraulic cylinders at each yoke tip. The hydraulic cylinders supported the weight of the transition structure while the necessary metrology was performed to ensure that the elevation axis was horizontal, parallel to the axis of the yoke arms, and intersected the azimuth axis within required tolerances. Once positioned, the saddle assemblies were secured to the yoke tips, and an axial preload of 20 tons was applied to the bearings to ensure they were seated properly in their races.

Installation of the Knuckle-Boom Crane, August 2010, and Counterweights, September 2010

The first item installed on the transition structure was a knuckle-boom crane mounted in a custom-designed frame (Figure 25). This frame sat on two beams that straddled the opening in the front of the transition structure through which the RF box would be installed. The center-mounted crane was a slightly customized articulating (or knuckle-boom) crane, typically found mounted on trucks used for delivering drywall or similar materials. This "crane-in-a-box" solved the problem of installing the new primary reflector surface (subframes) onto the new backstructure (see later section). Preinstalling the subframes or using the large site crane to position them was not an option because the subframes could not be installed until the radome was recapped to prevent damage to the subframes from wind or hail.

Equipped with several hundred feet of cable, the knuckle-boom crane, capable of lifting 1500 pounds at a 75-foot radius, would be able to lift the subframes from the floor of the radome and place them in their correct locations on the backstructure. When the surface installation was complete, the 10,000-pound crane would fold up into the 8 × 8–foot footprint of the RF box and be extracted out the back of the antenna by the antenna's overhead hoist.

Despite its 85-ton weight, the steel transition structure would not provide the necessary counterweight to balance the new 120-foot-diameter backstructure. Two large ballast containers built into the aft end of the transition structure were designed to be filled with concrete. Changes to the antenna design since the sizing of the counterweight containers had increased the antenna's weight, making it necessary to procure extra-dense concrete and fill at least one of the containers to the brim. The total weight of concrete in the top and bottom containers was 22 and 20 tons, respectively.

Temporary Building Removal, Quadrapod Installation, and New Dish Lift, July–September 2010

With the knuckle-boom crane installed, the transition structure was ready to receive the new backstructure. The backstructure is an all-welded aluminum assembly that is stiffness-optimized so that when it deforms (from gravity), it retains its parabolic shape, thus making it possible to compensate for deformation simply by adjusting the position of the subreflector to match the new focal point. The construction is a truss structure, in which the members are predominantly round tubes of a variety of diameters and wall thicknesses selected to match the desired stiffnesses (Figure 26). The tubes connect to one another at common junction points through an arrangement of

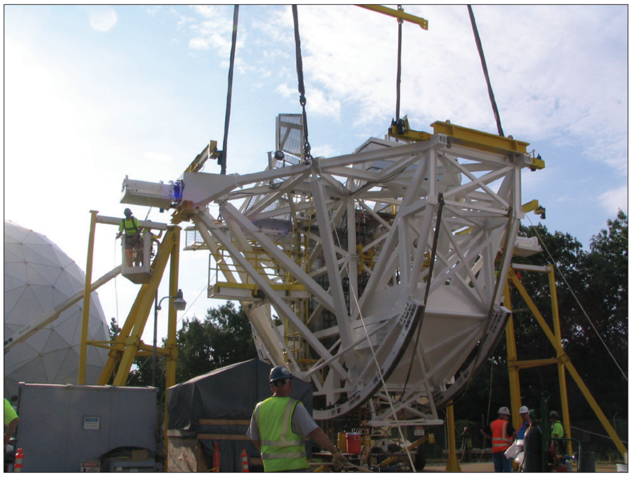

FIGURE 24. The completed transition structure is lifted off the temporary tripods, ready for installation on the modified yoke structure.

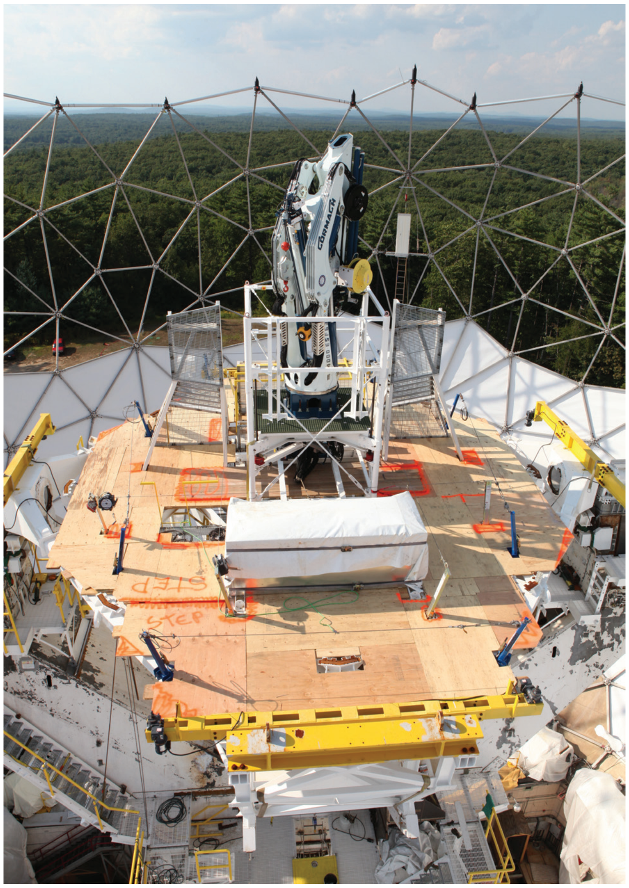

FIGURE 25. The knuckle-boom crane and two personnel platforms project above the front face of the transition structure prior to the installation of the new backstructure. Plywood decking has been installed to make a safer work surface while preparing for the backstructure installation.

FIGURE 26. The first two radial rib sections are installed on their assembly stands inside the temporary building. Note the workers and the 8-foot stepladder for scale.

FIGURE 27. This node point has 13 connecting elements.

flat plates welded together to form a cluster node. The complexity of the cluster nodes varies from minimal (only three or four members meet) to extreme (up to 16 members of many sizes join) (Figure 27). The resulting geometry demanded precision jigs to hold the variety of plate members in place during the complex welding required to access connection points deep within the joint.

The backstructure can be functionally separated into three major components: the torque ring, the radial ribs, and the outriggers (Figure 28). The torque ring, roughly toroidal in shape, is located at the vertex of the dish and is the central hub to which all other components connect. The radial ribs make up the greatest fraction of the surface area, extending radially outward from the torque ring. Together the ribs and torque ring provide mounting points for the 104 individual subframe assemblies that make up the primary reflector. The four outriggers support the quadrapod for the secondary reflector, and though each is interwoven inside a radial rib assembly in each quadrant, they are not in contact with the ribs and are mechanically and thermally independent. This design isolates the secondary reflector's load path from the primary reflector's supports, preventing much of the localized surface deformation found in other antennas. As with the transition structure, the components were assembled and welded at a fabrication shop up to the point where they were still transportable (albeit as oversized loads), and then joined together at the site.

The backstructure was integrated inside a large steel and fabric temporary building on the concrete pad near the radome. This building enabled aluminum welding to continue uninterrupted throughout the winter and in windy conditions that would otherwise have interfered with the creation of high-quality welds. Inside, on a support skeleton of pillars and scaffolding (Figure 26), the preassembled pieces were installed, aligned with a laser tracker, and then joined to their neighbors by a series of interstitial tubes. Once complete, the connecting flexure between the backstructure and the transition structure was installed.

To avoid thermally induced deformations between the steel transition structure and the aluminum backstructure, the engineering team developed a flexure configuration that is stiff in axial and lateral directions (along and orthogonal to the boresight axis) but compliant to radial growth resulting from differential expansion between the dissimilar metals. The flexure, or reflector support struts (RSS), comprises 16 legs, with eight connection points on the transition structure and eight on the backstructure. The circular sawtooth configuration provides stiffness in the loaded directions, while permitting the ends of the legs to flex radially (Figure 29). Each RSS leg has an aluminum section, welded to a node in the torque ring, and a steel section, bolted and then welded to pads on the front face of the transition structure. The interface between the two sections is a bolted joint with

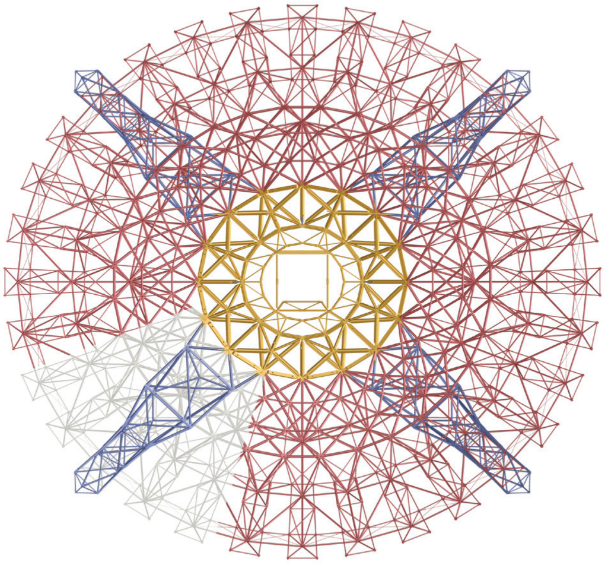

FIGURE 28. The computer-aided design (CAD) image shows the three major components of the backstructure: the torque ring (yellow), radial ribs (red), and outriggers (blue). A section of the radial ribs has been dimmed to show how the outriggers connect directly to the torque ring.

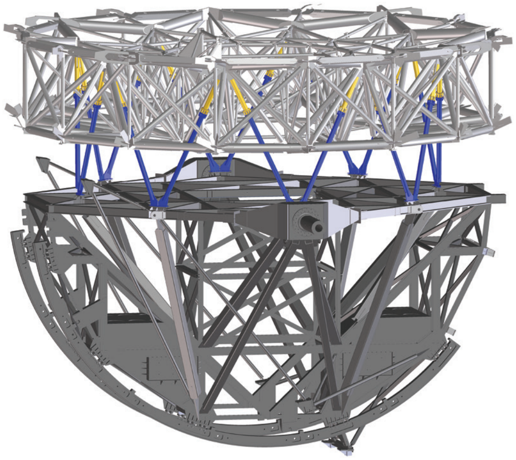

FIGURE 29. The reflector support struts (blue and yellow for the steel and aluminum sections, respectively) join the transition structure to the backstructure while providing isolation from differential thermal expansion.

a stainless steel spacer for galvanic corrosion resistance. To verify the strength of the RSS legs, one was tested on a large compression testing machine; it survived a 116,000-pound load, well above the maximum design load of 45,000 pounds (Figure 30).

Because alignment of the RSS to the mounting pads on the transition structure was critical, a template was built under the backstructure on the floor of the temporary building to simulate the mating surfaces of the transition structure. Once the RSS legs were all installed, this template was carefully disassembled and used to lay out the mounting points on the transition structure to ensure a perfect fit.

Next, the temporary building was removed to expose the new backstructure for the first time (Figure 31). To minimize the risk of damage to the newly completed structure, the building was dismantled away from the structure. The building was jacked up, set on rollers in a guide track, and rolled forward 40 feet at a time. Once the building was clear of the backstructure, two 20-foot-wide sections of the building could be disassembled without the crew having to work above the backstructure.

The backstructure was now ready to receive the quadrapod assembly, the secondary reflector‘s support struc-

FIGURE 30. The 12-foot-long reflector support struts were tested to more than 200% of the design load in both tension and compression in Lehigh University’s testing machine (note the person on floor for scale).

FIGURE 31. (a) Removal of the temporary building involved setting the building on rollers and rolling it into the parking lot for removal to minimize risk to the newly built backstructure seen in the background in (b).

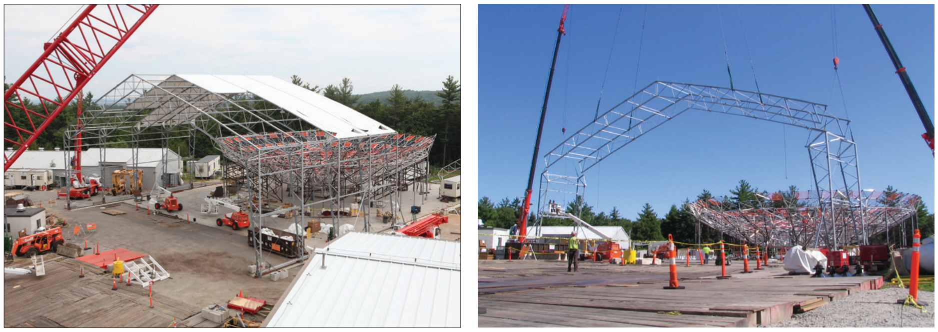

(a) (b)

FIGURE 32. The new backstructure is carefully lowered into position on top of the waiting transition structure.

FIGURE 33. The rails and dolly for the RF box insertion system are raised up in preparation to be threaded down into the transition structure.

ture that ties into the four independent, but interwoven, outriggers. The quadrapod consists of four planar trusses that meet at their peak in a box-like structure known as the apex. The apex supports the secondary reflector (subreflector) via six linear actuators (a hexapod arrangement) that control the position of the subreflector in all six degrees of freedom. The apex and quadrapod legs had been assembled around a 30-foot-tall tower built in a field adjacent to the temporary building. With the temporary building removed, the quadrapod and apex were lifted as one piece into position onto the backstructure, where the four quadrapod legs were welded to the mating interfaces on the ends of the outriggers. To protect the subreflector and electronic actuators from weather, they were not installed until after the major integration was complete and the radome cap replaced.

To prepare for the lift of the entire backstructure assembly onto the transition structure, a dry run was performed a few days prior to the planned lift date. This dry run was unique among all the lifts and was necessary because of the tight tolerances required to mate the backstructure to the transition structure.

Not only was the final positioning of the eight RSS mounting pads critical, but the backstructure would also have to be lowered down onto the transition structure without disturbing the knuckle-boom crane and two RF box platforms, all of which project well above the front face of the transition structure. The resulting clearances between these projections and members of the aluminum backstructure were as little as 3 inches in some cases. Because of the height of the knuckle-boom crane, the risk of damage to the backstructure from an unexpected swing could occur when the backstructure was still as high as 25 feet above the transition structure. These tight clearances, combined with the large sail area

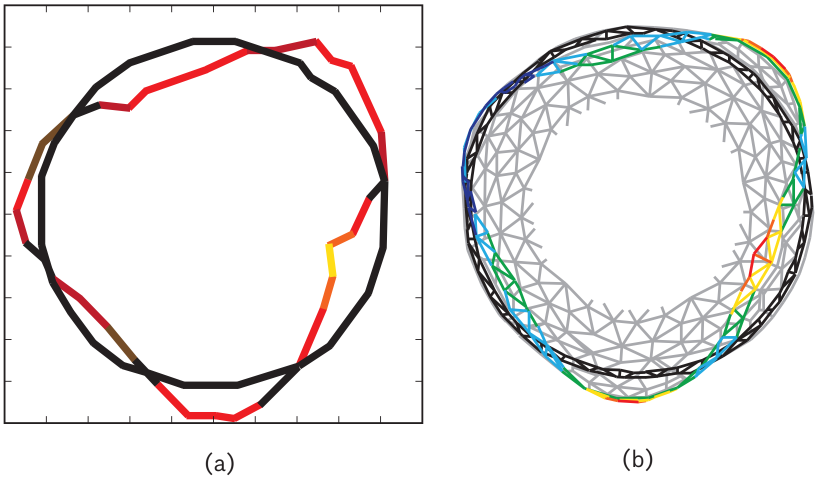

FIGURE 34. (a) Metrology (exaggerated for clarity) performed while the radome was uncapped showed a good match to the predicted (also exaggerated) deformed shape determined by the finite element analysis model (b). The actual magnitude of the deformation was within the capabilities of the self-alignment features built into the mating node halves.

of the backstructure, required exceptionally calm winds during the lift and the added control of a series of crossed come-alongs (cable pullers) fastened between the transition structure and the backstructure once the two were within 20 feet of each other.

The ratchet straps, operated by ironworkers at the front face of the transition structure, provided lateral and circumferential restraint as the backstructure was slowly lowered, preventing the backstructure from swinging or spinning about its axis and making contact with any of the projecting structures. This careful coordination between the crane operator and the teams of ironworkers was the focus of the test lift, and proved that the crossed ratchet straps could adequately control the position of the 120-foot-diameter, 30-ton backstructure. The actual lift, completed on the morning of 2 September 2010, was successful largely because of the careful planning and additional time taken for the test lift (Figure 32).

RF Box Insertion System Lift, September 2010

The addition of the Octagon onto the front of the RF box enables the once separate functions of radar and radio astronomy to be merged into a common RF box. However, an overhead hoist system similar to the one used on the legacy antenna was still needed to lower the RF box for major maintenance tasks. Greater RF box weight, more rigorous industry standards, and minimal available headroom demanded a highly customized solution. A regional manufacturer was able to base the hoist design loosely on one created for the removal and maintenance of roof-mounted air-conditioner units on subway cars. The design, similar in function to that of the legacy hoist system, comprises a dolly, with two electric winches, that rides on a pair of 37-foot-long steel rails. The rails, in turn, can be driven along rollers to cantilever out the rear of the transition structure and provide a clear path for the RF box to be lowered to the ground. The rollers had been preinstalled in the transition structure while still on the temporary stands, and the two rails with the associated dolly were lifted and carefully guided into the roller cradles and secured in place (Figure 33).

Radome Recapping, September 2010

With the major integration of the new antenna complete, the final large lift was the reinstallation of the radome cap. The successful placement of the radome cap on the temporary support piers in the parking lot had proved that the analysis of the radome cap deformation when subjected to lifting forces had been correct. For the reinstallation, however, not only the deformation of the cap but also the deformation of the top edge of the remaining radome was important. Beginning the day after the radome cap removal, a series of measurements had tracked the positions of the node halves along the exposed edge of the radome. These surveys showed that the split-line nodes did in fact deform from a circular shape into a three-lobed shape, but that the magnitude of the deformations was within the capabilities of the alignment cones on the split-nodes (Figure 34). Even so, a contingency plan was developed to utilize come-alongs to

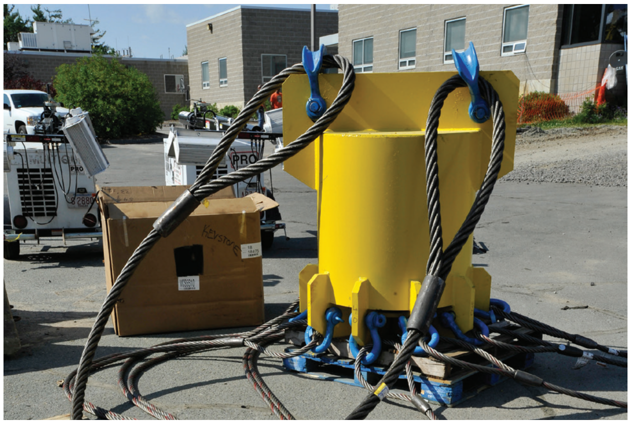

FIGURE 35. The 6-foot-tall lifting fixture for the radome cap ensured that all 10 lifting lines had a common action point and prevented bunching of the slings.

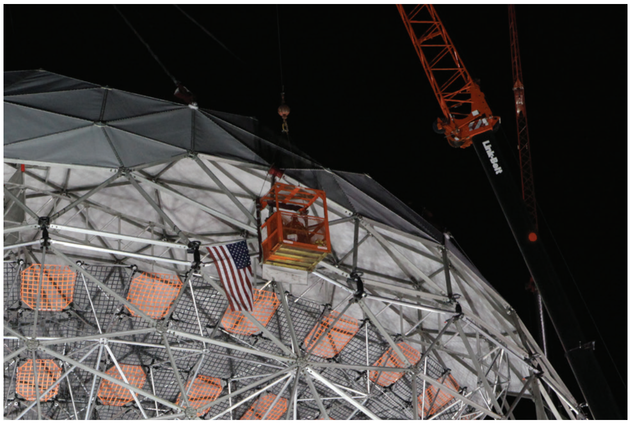

FIGURE 36. Workers in aerial lifts and crane baskets guide the radome cap onto the truncated radome.

pull the outwardly splayed edges of the radome together, thus reforming the circular shape.

The night before the planned lift, preparations began with the rigging of the radome cap to the custom-built lifting fixture (Figure 35). As with the removal of the cap, the lifting fixture and the 10 straps connected to the lifting nodes on the radome cap were designed to ensure equal distribution of the lifting force and to direct the lifting forces tangent to the radome cap to minimize distortion. The hold-down bolts installed in the split-nodes to prevent uplift of the cap during high winds were removed. Where previous lifts had relied upon workers to control the lateral motion of the lifted item with long taglines, the large sail area of the radome cap meant that the taglines would need to be routed through heavy concrete Jersey barriers to ensure that the load could be controlled. These barriers had been set up around the perimeter of the radome, and the movement of tagline operators was carefully choreographed ahead of time to ensure that cables would not become snagged on any nearby structures or get entangled with a neighboring tagline.

Just prior to the pre-dawn liftoff, the ironworkers affixed an American flag to one of the radome beams in a tradition known in the industry as "topping off." As the cap passed over the top of the new antenna and began to be lowered, half a dozen ironworkers in aerial lifts and crane-suspended man-baskets ascended to the edge of the radome to monitor the engagement of the alignment features on the split-nodes (Figure 36). The alignment features adequately corrected the shape of the lower edge of the radome, and the Haystack radome was successfully rejoined after a 15-week integration period.

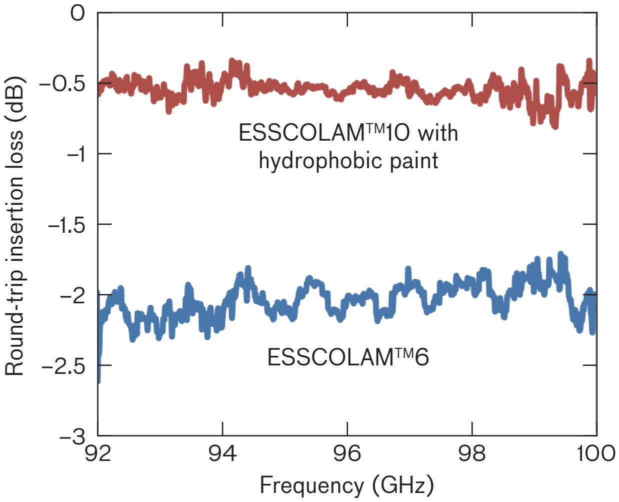

FIGURE 37. Measurements of the new three-ply ESSCOLAM™10 showed significantly better membrane performance at W band than the performance of the legacy two-ply ESSCOLAM™6.

While the metal space frame of the Haystack radome was unchanged during the upgrade process, the radome membranes ("skins") did require replacement in order to minimize loss at the new 96 GHz operating frequency. The new membrane material is three-ply ESSCOLAM™10 (a proprietary polymer material) with a hydrophobic coating on the outer layer to repel water that would otherwise attenuate the W-band signals (Figure 37). The skins were fabricated and cut to the 15 unique shapes that compose

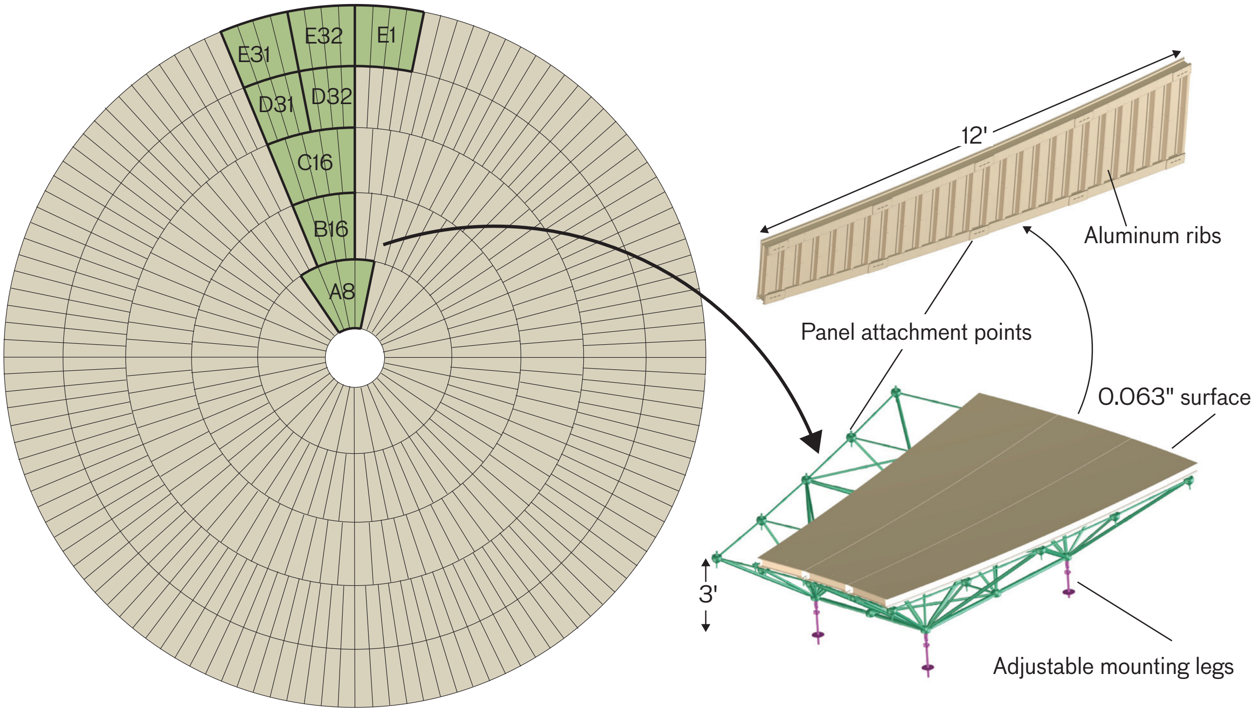

FIGURE 38. The primary reflector with one of each ring type is highlighted. The breakout images show a subframe assembly with mounting hardware and the backside of a surface panel with stiffening ribs.

the radome openings; then, extruded aluminum edging was epoxied and crimped in place to permit installation. The skins were stretched across the 930 triangular openings and secured to the radome beams with a new set of 85,000 custom T-bolts.

The membrane replacement was done in three phases and was driven by the need to minimize the wind loading on the lower half of the uncapped radome. Prior to the removal of the radome cap, the membranes had been removed from a region extending from the split-line down to approximately a third of the height of the radome. The resulting reduced surface area ensured that the uncapped radome would not be damaged by high wind loads. The skins on the radome cap were replaced while the cap was on its temporary support piers in the parking lot in order to minimize the height at which work would have to be performed. At the same time, the membranes along the bottom third of the radome were replaced.

Because of wind constraints, the middle third of the radome could not be re-skinned until the cap had been replaced. Once the cap was safely replaced, the priority was the completion of the re-skinning process in order to enclose the newly installed antenna and begin installing the surface panels, which were deemed too sensitive to risk being exposed to the weather.

Subframe Installation, October 2010–January 2011

In order to move from X band to W band, the quality of the primary reflector surface had to improve to approximately 100 μm rms (at a “rigging angle” of 25°, with allowances for gravity deformation at other angles). Along with the newly designed backstructure and the isolated outriggers to support the secondary reflector, this requirement was met by segmenting the primary surface into 432 individual panels on 104 subassemblies known as subframes. The subframes are arranged in five concentric rings (labeled A through E). Each subframe is mounted to the backstructure by four adjustable legs and supports four or five surface panels (Figure 38).

Each subframe is a trapezoidal aluminum truss structure, approximately 12 feet square and 30 inches tall with up to 39 nodes connected by up to 262 tube segments. By using an assembly jig, workers located the

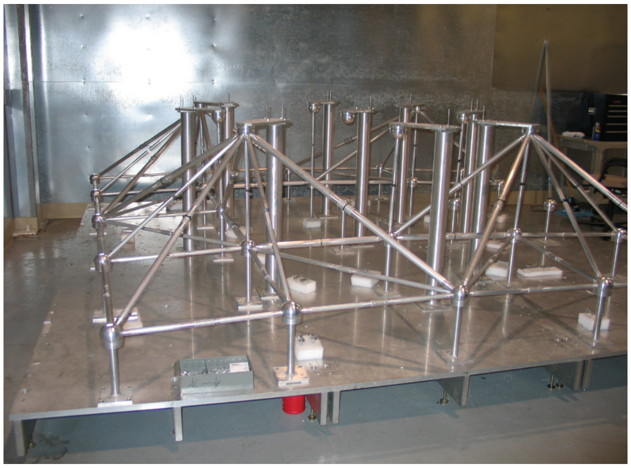

FIGURE 39. A partially completed subframe is assembled upside down on an assembly jig.

FIGURE 40. Completed subframe trusses await panel installation. All 104 subframe assemblies were stored on racks in an airplane hangar until they were transported to the site.

FIGURE 41. A subframe is secured to the steel frame on the transport trailer and then pivoted to fit inside the 8-foot-wide trailer body.

nodes in space before the tube segments were installed (Figure 39). The nodes incorporate mounting points for the surface panels on top and provisions for the four threaded rod assemblies that interface with the backstructure. The threaded ends of the tubes were coated with epoxy prior to inserting them into corresponding tapped holes in the nodes. After all connections were made and the epoxy had set, the completed subframe was removed from the assembly jig.

The primary reflector panels are thin (0.062 inch) aluminum sheets formed on vacuum molds with stiffening ribs epoxied to the backside to hold the deformed shape. Installation of the panels onto the subframes was performed in a custom-built, thermally stable room to minimize distortion of the surface panels. A laser radar was used to measure the four (or five, in the case of the larger subframes) surface panels as they were mounted via 10 adjustable rods. The measured positions were compared to the ideal computer-aided design (CAD) model and adjustment commands were generated for the workers. This process enabled placement of the panels within 16 μm of their ideal positions [2]. The completed subframe assemblies, whose weights range from 350 to 600 pounds, were stored on 35-foot-tall racks inside an airplane hangar until the new antenna was installed and the radome fully enclosed (Figure 40).

The completed subframe assemblies were transported 45 minutes to the construction site on a pair of custom-built enclosed trailers that prevented damage from weather or road debris. Each trailer could carry a single subframe assembly on a mounting fixture that angled the 12-foot-wide subframes such that they fit within a standard trailer width (Figure 41). To support the installation goal of six subframes per day, a temporary storage shelter for the subframes was built in close proximity to the Haystack radome to act as a buffer in case of disruption to the supply chain. A clear-span tent capable of storing up to 20 subframe assemblies was erected on the concrete pad where the backstructure had been assembled. From this tent, the subframes were moved by forklift into the radome and up onto the roof of the control room inside the base of the radome. Here they were loaded onto large dollies, rolled to the center of the roof, and prepped to be lifted into position on the surface of the backstructure.

With the radome cap installed, the gap between the edge of the backstructure and the inside diameter of the

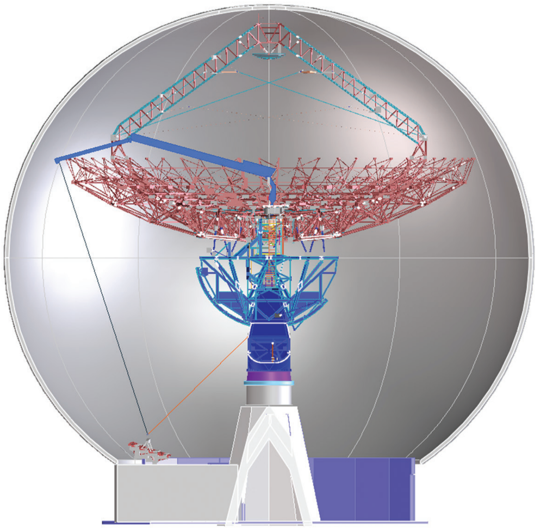

FIGURE 42. The cross-sectional CAD view shows the articulating crane lifting a subframe from the control room roof with the assistance of a winch mounted on the yoke.

FIGURE 43. A subframe is lifted off the control room roof.

radome is too small for a subframe to fit through, so a small section of one of the backstructure ribs had been left off during assembly to provide an opening large enough to pass a subframe through. This notch was at the 6-o'clock (bottom) position of the dish, which coincided with the centerline of the control room roof. The knuckle-boom crane, which had been folded up no larger than the RF box, now unfolded and telescoped until the tip of the jib was directly over the backstructure notch. The lifting line was lowered and simultaneously pulled in toward the center of the radome with the help of a tagline wound around a capstan winch located at the base of the yoke. This tandem line technique allowed the hook to be lowered at an angle of approximately 20° from vertical, placing the hook directly over the subframe assembly waiting on the control room roof (Figures 42 and 43).

The top surfaces of the panels do not have any lifting features, so custom lifting straps had been fabricated from seatbelt webbing, a single ply of which was just thin enough to fit through the 3 mm gaps between adjacent panels. The straps, carefully threaded between panels, were used to lift the subframe from the same four nodes that would be attached to the backstructure. Because the panel gaps were too small to pass the double-thickness loop ends through, the straps had to be cut from below once the panel was installed. Each panel was guided into position by a team of ironworkers working in nets that had been installed while the backstructure was still in the temporary building. Workers in the nets had to be cautious when moving around the backstructure as some of the aluminum tubes have such thin walls that even leaning against them could result in damage. As the surface began to take shape, the space available for the workers was restricted to small triangular "tunnels" formed between two adjacent subframes (Figure 44).

Starting near the center, and opposite the notch in the backstructure, the panels were positioned based on guidance from a laser tracker located near the vertex of the dish (Figure 45). Once the subframes were freed from the crane, their "rough alignment" began with the installation of a pair of temporary targets in tooling holes on the top surface of two of the aluminum panels. On the basis of the feedback from these measurements, the crew of ironworkers adjusted the subframes vertically and laterally to within approximately 1 mm of its ideal position by using jam nuts on the threaded mounting rods to set the height and customized tooling to correct the lateral position. Once positioned, the subframe was secured in place with a large fender washer and nuts on the underside of the backstructure attachment point.

Halfway through the subframe installation process, the project experienced a major setback. During the placement of a subframe at the perimeter of the dish surface, the knuckle-boom crane malfunctioned and dropped the heavy steel rigging equipment onto the surface of the just-installed subframe, denting two of its four surface panels. Although the resulting month-long failure investigation

FIGURE 44. Workers in the nets must be careful around the fragile aluminum tubes above and below them.

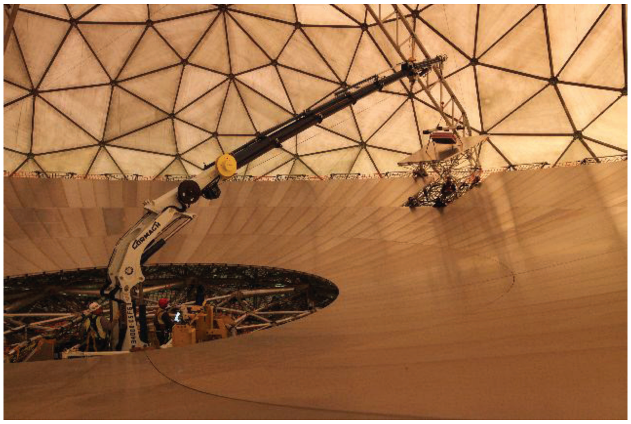

FIGURE 45. A subframe is lowered into position with the knuckle-boom crane.

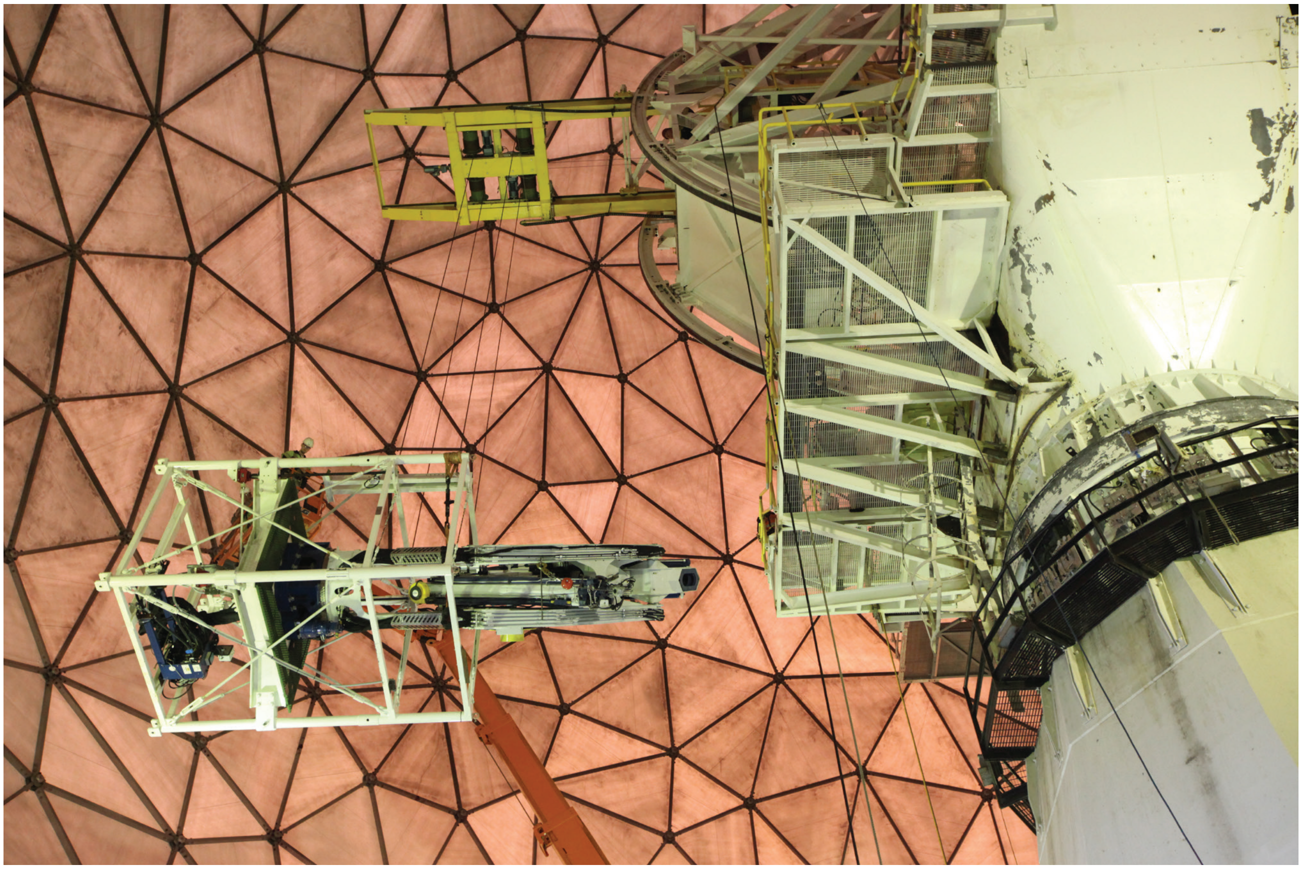

FIGURE 46. The RF box insertion system (RFBIS) hoist lowers the folded-up knuckle-boom crane down to the floor after completion of the subframe installation.

did not conclusively determine the cause of the malfunction, it appears likely that moisture in an electrical enclosure may have led to a short circuit in the remote-control system. When work resumed, the crane operator, who had previously been able monitor the entire lift from the dish's edge, could no longer use the remote-control unit but had to control the crane from the hydraulic valves at its base and rely on hand signals or radio communication from spotters located at key vantage points.

Because the last two subframe assemblies relied upon the notched part of the backstructure for support, they were lifted and temporarily set on top of already installed panels while the notched section was emplaced. To disconnect and reconnect those subframes from the crane, a remotely operated lifting magnet hoisted each subframe up through the notched section and set it down on foam pads placed on several interior panels. The steel spreader bar and associated rigging equipment were lowered down onto more foam pads designed to prevent the equipment from damaging the aluminum panels. With the weight released, the lifting magnet was remotely de-energized, and the crane was used to lift the missing notch into position. The last two panels were re-engaged by carefully lowering the lifting magnet onto the steel spreader bar and energizing the magnet. The panels were then positioned and their lifting straps cut from below, as with the other 102 subframes. After the final subframe was placed, the crane was once again folded up into its stowed configuration in preparation for its removal from the antenna.

Knuckle-Boom Crane Removal, February 2011, and Optics Box Installation, March 2011

With the antenna's primary surface fully installed and the knuckle-boom crane stowed, the new HUSIR antenna was ready for its first rotation about the elevation axis. To minimize the risk of inadvertent motion or a runaway caused by an imbalance, this rotation was performed by using the hand-crank mechanism rather than the new control system. A supplemental system of cables between the rotating and stationary components was also installed in order to provide a redundant restraint system.

The removal of the knuckle-boom crane would also double as the first full-scale, end-to-end test of the RF box insertion system (RFBIS) (Figure 46). The lifting points built into the knuckle-boom crane were used to transfer the weight of the crane to the RFBIS, and the mounting beams that had supported the crane were removed. The RFBIS dolly then traversed beyond the aft end of the transition structure and cantilevered out nearly 20 feet. After the 8-ton knuckle-boom crane was lowered 85 feet to the floor, the RFBIS was used to lift a surrogate RF box (known as the optics box) into position.

The optics box, a retrofitted version of one of the alternate RF boxes for the old Haystack antenna, was ballasted with water tanks and steel plates in order to more closely match the weight and center of gravity of the new RF box. This arrangement allowed the antenna to be more finely balanced for future motion testing while work continued on the actual RF box on the ground. The optics box also provided a mounting interface for the laser radar that would be used to measure the position of the secondary reflector (subreflector) when it was installed on the apex.

Laser Radar Lift, Surface Alignment, and Subreflector Lift, March–May 2011

During the installation of the subframes onto the backstructure, a rough alignment had been performed in order to set the subframes within approximately 1 mm of their final positions. However, the final surface required much better alignment to satisfy the demands of the new W-band system. Only a few metrology techniques were considered capable of performing the necessary measurements across the surface of the entire 1/3-acre surface. The measurements had to be taken with sufficient speed to avoid thermal transients and required an accuracy better than 20 μm rms. A holography-based measurement system was considered to be the best possible system because of its quick measurement time, high spatial resolution, and high accuracy. However, such a system requires the use of the receivers in the RF box, which was not yet available, and a significant development effort, which was under way as a risk-reduction effort but not yet mature. The next best metrology system was the laser radar that had previously been used to align the panels to the subframes.

The laser radar uses a gimbaled scanning mirror to achieve a field of coverage of approximately ±45° in elevation and 360° in azimuth. Previous experience had shown that the loss of reflected energy prevented the use of a laser radar on aluminum surfaces at low incidence angles. This constraint limited the possible mounting locations to areas directly along the boresight axis. Within the con-

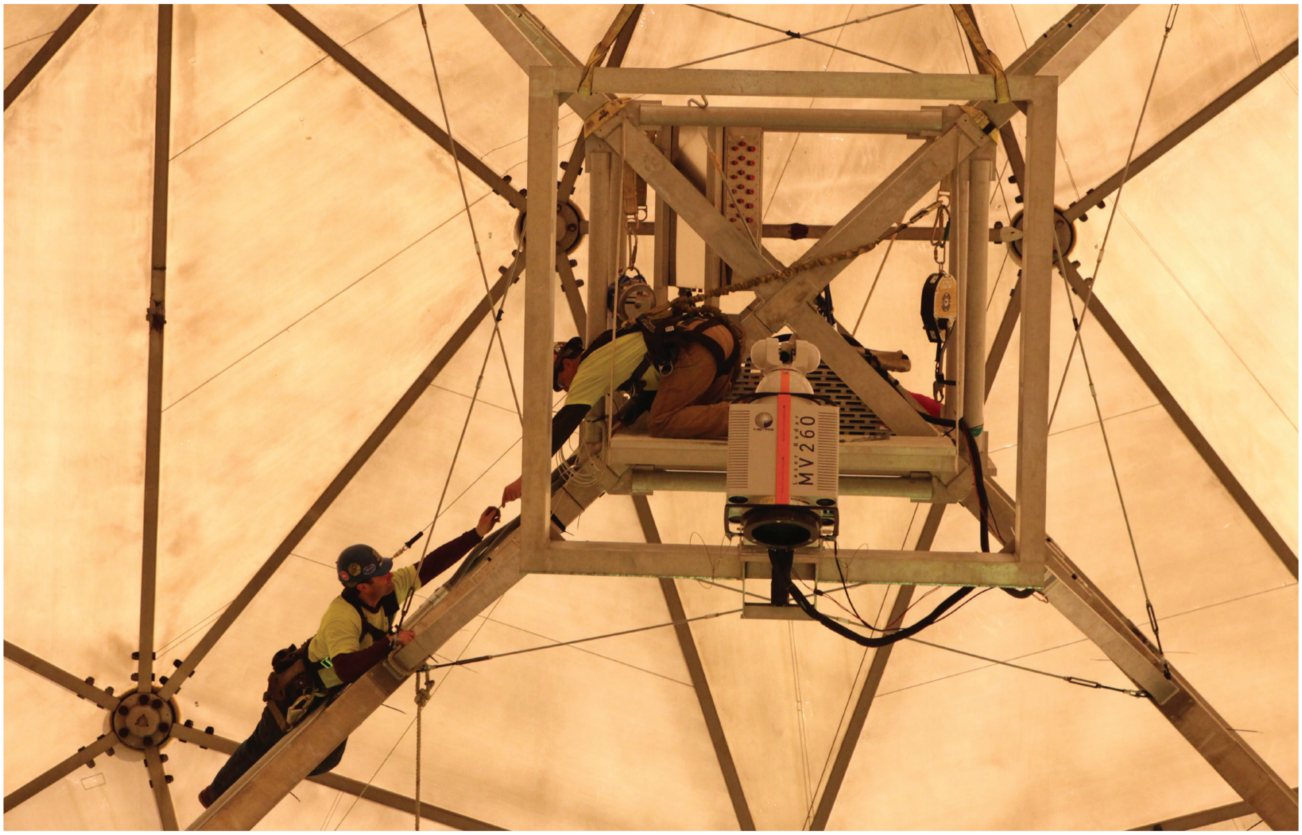

FIGURE 47. Workers secure the laser radar bracket to the quadrapod legs in front of the apex.

fines of the radome, no location provided the laser radar with sufficient standoff distance to measure the whole surface from a fixed vantage (the top and/or bottom of the dish would be outside the vertical bounds). The best available mounting location was determined to be a point near the apex, just in front of where the subreflector would be installed. This location had two advantages: it was on the antenna structure (not on the radome where vibration or wind deflection would exceed the measurement tolerances); and it could exploit the isolation provided by the independent support of the outriggers. The location's drawbacks were that it would compel the laser radar to tilt halfway through a measurement in order to survey the entire surface and that it would require the laser radar to travel with the antenna as it moved from the measurement angle of 25° to zenith, where the adjustments to the subframes would be performed.

The laser radar could not be installed on the apex by employing a conventional crane operation because the primary reflector effectively blocks any access from the base of the radome to any point in front of the dish surface. Accessing the old Haystack subreflector had entailed removing one or more radome panels and lifting items from outside the radome with a large crane. To undertake a similar operation for the laser radar was undesirable because of the cost and complexity of removing the recently installed radome panels, as well as the associated susceptibility to inclement weather. The alternative solution was to utilize a radome node as a lifting point, with a ground-mounted hoist controlling the hook via a series of pulleys on the side of the radome to keep the cable out of the swing path of the antenna. The laser radar and its mounting bracket were set on a temporary platform attached to the lower edge of the radome directly below the lifting node while the antenna was facing the opposite direction; then, the antenna was rotated in azimuth until the apex was in line with the lifting node. Finally, the ground-based winch lifted the laser radar to the apex, where it was secured to the antenna (Figure 47).

Over the course of the next month, the fine alignment of the antenna progressed, and the surface error was reduced from more than 1900 μm to approximately

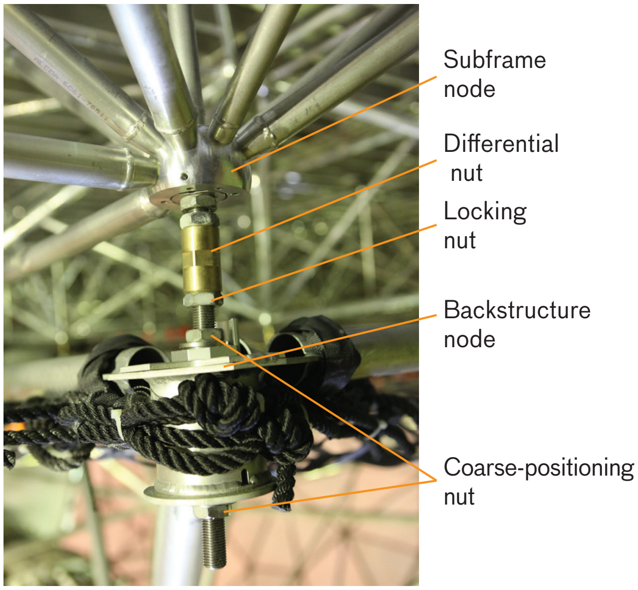

FIGURE 48. A photograph of a typical backstructure node with a subframe mounting foot installed shows the black ropes that support the personnel netting.

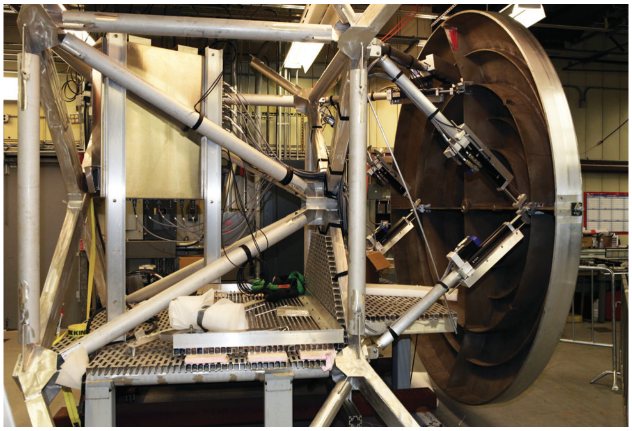

FIGURE 49. The subreflector is installed on the apex for control system testing prior to integration.

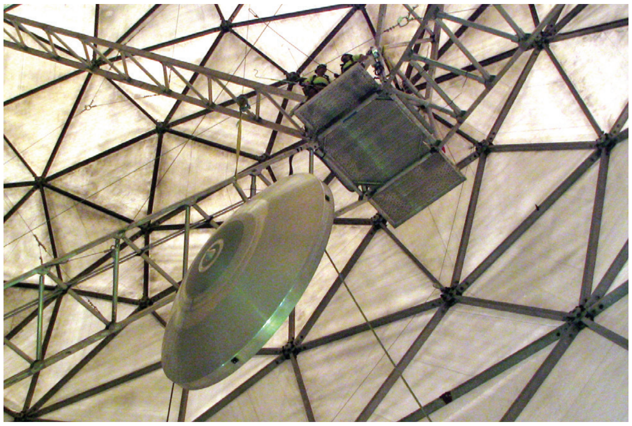

FIGURE 50. The subreflector is lifted from the lower edge of the radome to workers waiting on the apex platform.

150 μm. To minimize thermal gradients on the structure, the antenna was parked at the rigging angle of 25° and measured during the overnight hours when diurnal temperature changes were smallest. Then, a list of adjustments for each of the four mounting rods for all 104 subframes was generated on the basis of the offsets between the measured surface and a best-fit parabola of the correct parameters. During the day shift, with the antenna at zenith, several teams of workers crawled through the nets to adjust the surface height, first in coarse steps and then in fine increments. For a detailed discussion of the alignment process, see the article "Optimizing the HUSIR Antenna Surface" in this issue of the *Lincoln Laboratory Journal*.

The adjustment mechanism consists of a differential nut that connects two threaded rods of slightly different pitch (threads per length). Turning the differential nut one-sixth of a turn (one "flat" on a hex nut) moves the surface above by 25 μm. For coarse adjustments, this differential nut is bypassed, and the nut securing the subframe to the backstructure (Figure 48) is turned to raise or lower the subframe in increments of 0.015 inch (380 μm) per "flat of the nut."

Progress was swift early in the adjustment process when the surface errors were comparatively large. However, when the measurement process began to reach a noise floor, it was determined that the laser radar was losing calibration as a result of being operated in various orientations. Consultation with the vendor could not convincingly show a means of mitigating this effect. Since the current state of the antenna was considered adequate for proceeding with preliminary antenna motion and RF testing, the project team decided that these problems would be addressed with a subsequent alignment effort when the holography system was ready for use.

The laser radar was removed from the antenna and mounted to the front of the optics box for a clear line of sight to the apex on which the subreflector would be mounted (Figures 49 and 50). The subreflector, a 1000-pound, 10-foot-diameter aluminum hyperbola, is supported by a hexapod arrangement of six linear actuators. The actuators each have 200 mm (7.8 inches) of

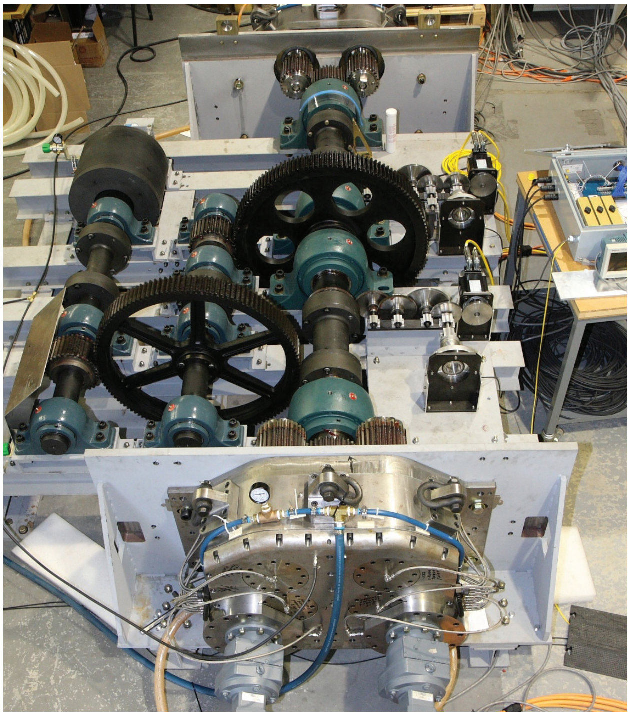

FIGURE 51. The elevation simulator is used to coordinate the interaction of all four elevation pinions and tune the control system with an equivalent inertial load.

stroke and include encoders with 1 μm resolution for precise positioning. The subreflector is moved along the boresight axis to compensate for the change in focal length of the primary reflector as the antenna moves in elevation; it can also tip and tilt to illuminate the off-axis radio-astronomy feeds on the front of the Octagon.

The subreflector has four tooling balls mounted around the perimeter at known locations. From the front of the optics box, the laser radar could combine those four points with other fiducial markers on the dish surface to determine the relationship between the primary and secondary reflectors.

Control System Testing and Hydrostatic Bearing Failure, May–August 2011

The subreflector installation represented the end of the major construction phase and the beginning of control system testing. Among the first tasks was a penultimate balancing of the elevation axis; a final balancing would be required when the temporary optics box was replaced with the actual RF box. Counterweight adjustments were determined by measuring the torque needed to drive the antenna up or down at various elevation angles. Because of the previously noted increased mass of the system, the built-in trim-weight locations would not provide enough room for the amount of additional counterweight needed. Therefore, several new trim-plate locations were created, and 5000 pounds of additional steel plates were added to the rear of the transition structure. The balanced antenna could now undergo control system testing to validate both the software models and the inertia simulator that had been built offsite to aid with tuning of the control system.

The inertia simulator was a large steel framework in which the motors and gearboxes were installed in an arrangement comparable to their actual mounting on the antenna (Figure 51). An 875-pound flywheel rotating at speeds up to 360 rpm represented the inertial load of the antenna. The simulator had been used over the past year to aid with dynamic performance models and the development of the counter-torque scheme used to eliminate backlash in both azimuth and elevation axes.

During typical tracking operations (at low acceleration rates), half of the pinions in a given axis drive the antenna while the other half provide a resisting torque. This technique ensures that the driven gear (the bull gear in azimuth or sector gear in elevation) is consistently loaded and eliminates any motion from the clearance between mating gear teeth. Combined with the low-friction hydrostatic bearing, the anti-backlash scheme permits the antenna to achieve tracking accuracy as low as 0.0005° (8.7 μrad). Only under high acceleration rates do the lagging pinions begin assisting the leading pinions, thus reducing tooth loads on the gears during the most stressing motions.

Prior to transitioning from manual control (hand cranking) to the new control system, the safety features of the new antenna were verified. The antenna has three layers of motion-limiting devices: software, electromechanical (limit switches that de-energize the drives), and mechanical (gas-filled buffer stops that bring the antenna to a controlled stop). Personnel safety measures, such as interlocks and emergency stops, were also extensively tested. The antenna's range of travel was verified to be 0–90° in elevation and 600° in azimuth (±300° from due south). Following a carefully planned incremental procedure, the antenna was slowly driven up to its maximum performance limits (acceleration rates and velocities of $1.5°/s^2$ and 5°/s in azimuth and $2°/s^2$ and 2°/s in elevation, respectively).

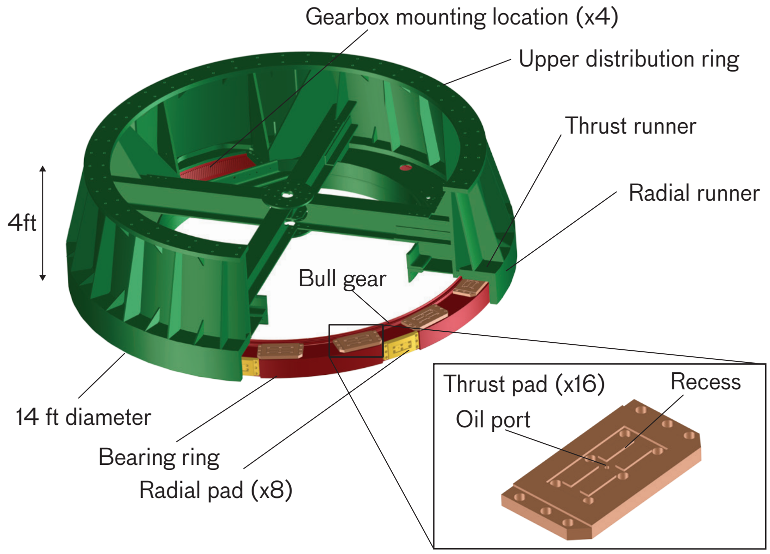

FIGURE 52. A CAD model of the key hydrostatic bearing components shows the thrust pads (bronze) and radial pads (yellow) mounted on the stationary bull gear (red). The pads exert force against the thrust and radial runners, respectively, which are parts of the rotating upper distribution ring (green).

On 9 August 2011, following four months of successful control system testing, the hydrostatic bearing that supports the entire moving structure experienced a dramatic failure. During a routine rotation in azimuth, the torque required to move the antenna suddenly spiked, a loud screeching noise was heard, and antenna motion stopped when the azimuth drives reached their maximum torque.

The hydrostatic bearing, part of the original Haystack antenna, had long been a great success. At its most basic, a hydrostatic bearing can be compared to a Kugel ball—the popular garden sculpture that has a sphere spinning freely on a film of water pumped from below. The benefit of a hydrostatic bearing over conventional bearings is the near elimination of both friction and stiction (static friction). This benefit contributes greatly to the ability of the antenna to maintain high precision while tracking at exceptionally low angular rates. While some antennas have utilized a Kugel ball–style spherical hydrostatic bearing (the Green Bank 43-meter antenna, for example), the Haystack bearing is a combination of a vertical (thrust) and radial bearing, built into the 12-foot-diameter bull gear (Figure 52).

When operating properly, the thrust bearing supports the entire 340-ton weight of the antenna structure on a film of oil approximately 0.005 inches (0.12 mm) thick. The oil is pumped under moderate pressure (1500 pounds per square inch [psi]) to each of 16 "thrust pads" evenly distributed around the top of the bull gear. Each thrust pad is a precision-machined block of steel with recessed channels to distribute the oil. The pressurized oil acts over the surface area of each thrust pad (9 × 14 inches) to lift an annulus (the thrust runner), which is part of the rotating superstructure. The oil overflows the pad and is drained under ambient pressure back to the pump reservoir. Approximately 30 gallons of oil per minute are required to keep the antenna "floating."

A similar arrangement of eight radial pads built into the outside of the bull gear is used to resist radial loads and keep the antenna centered about the azimuthal axis. These pads force the oil against a vertical section of the runner that overhangs the bull gear. Because of the smaller forces involved, these radial pads only require 3 gallons per minute at a pressure of 800 psi to keep the antenna centered.

The location at which the bearing became stuck was determined by calculating the load on each of the 16 thrust pads (based on their individual oil pressure) and then ascertaining where the "missing" weight of the antenna was. Whatever was causing the bearing to stick was supporting approximately 40,000 pounds of the antenna weight. To free the bearing, temporary hydraulic modifications were made to allow for increased oil pressure and flow to the thrust pads in the region of the "missing" weight. These modifications made it possible to reverse the motion of the antenna and rotate it so the affected region was between thrust pads, where the damage could be inspected and repaired. As the mating surfaces of the hydrostatic bearing are not readily accessible, visual investigations were carried out with borescopes snaked in from outside the bearing. The resulting images showed a region of the runner marred by deep pits, gouges, and

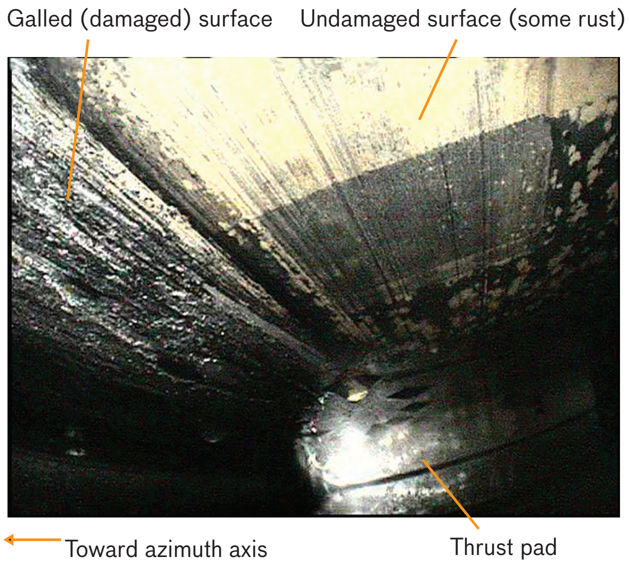

FIGURE 53. A borescope image of the thrust-runner surface shows the damaged portion on the left and the smooth portion on the right. The discoloration on the right is due to mild surface rust, likely from the integration period when the bearing was not being used. A thrust pad can be seen in the distance.

lumps (Figure 53). While the root cause of the damage was not yet known, it was obvious that the lumps would need to be removed for the bearing to operate again.

The only way to gain direct access to the runner surface and perform any repair work was to drill a hole through the 3-inch-thick vertical wall that forms the radial runner. With a 1.5-inch access hole in place, a laser profilometer was used to generate a very accurate surface map of the damaged area and to measure repair progress. The initial scans with the laser profilometer confirmed what the borescope had indicated: the thrust runner had a lump approximately 4 inches long (along the axis of motion) and 1 inch wide (radially), with a peak height of approximately 0.020 inches (Figure 54). Given the nominal clearance of 0.005 inches between the thrust pad and the runner, this finding suggested that the surface of the thrust pad was gouged by the lump, as it was unlikely that even the increased oil flow to the local thrust pads would have been able to generate enough lift to clear the full height of the lump.

Over several months, the damaged portion of the runner was repaired by grinding it smooth with diamond-encrusted files inserted through the access hole. Softer file

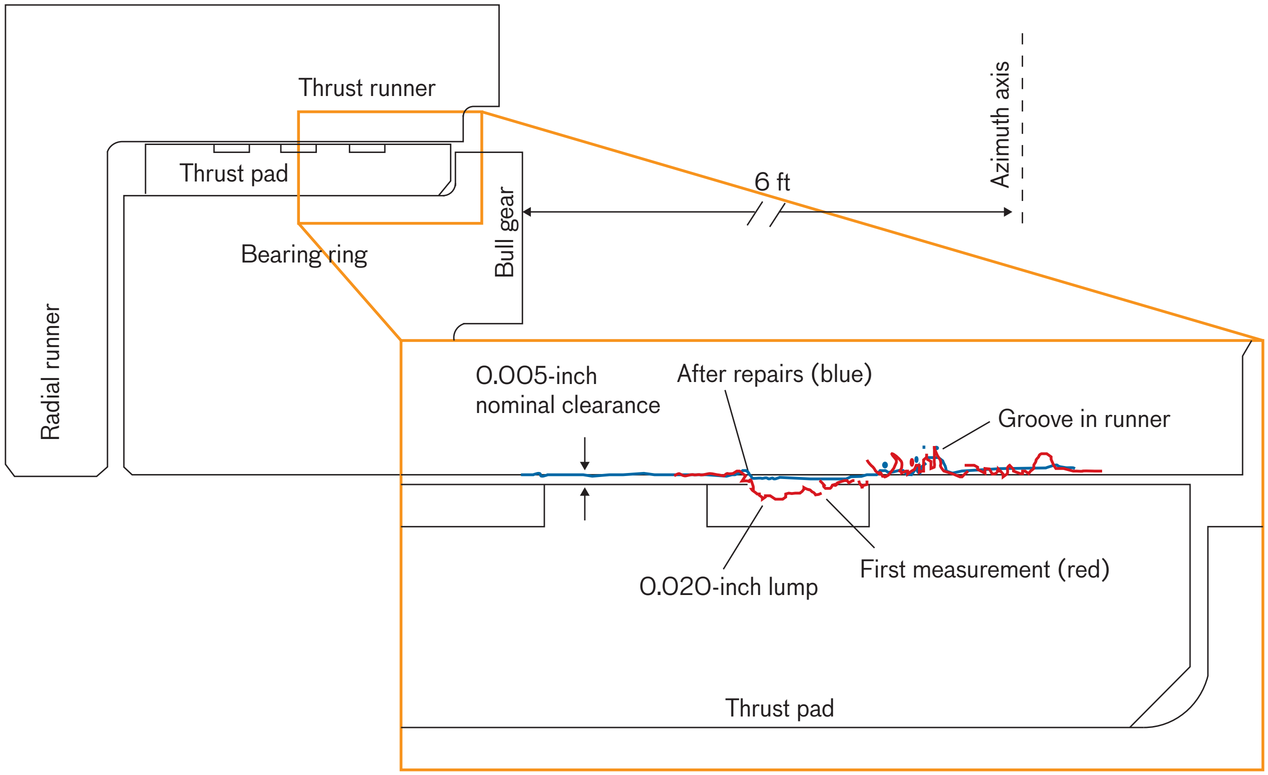

Vertical scale magnified 10x

FIGURE 54. An overlay of the laser profilometer scan on a CAD drawing shows the location of the lump in line with the innermost oil groove in the thrust pad.

materials had been unsuccessful at removing the lump, bolstering the growing suspicion that the lump was generated by galling between the moving surfaces. Galled material is generated when sliding surfaces under load begin to adhere to one another, leading to a transfer of material between the surfaces. The resulting material is effectively friction-welded and is typically very hard. In this case, the two sliding surfaces are both steel, heat treated for additional hardness, making the resulting galled material difficult to remove even with diamond files.

While the repair work progressed, an investigation into the binding incident showed that under certain conditions the nominally flat surface of the thrust runner was prone to localized tilting (the outer edge of the annulus being higher than the inner edge). Though the thrust pads are very stiff in the vertical direction (a doubling of the load only reduces the ride height by 10%), they have no moment-carrying capability (i.e., from one side of the pad to the other). The investigators concluded that the greater post-upgrade weight of the antenna caused more static deformation of the runner than previously assumed. By itself, this static deflection was not enough to cause the bearing to bind, as demonstrated by the four months of operation following the upgrade. However, the investigators also found that thermal gradients in the structure could exacerbate the static tilt, and a large temperature swing around the date of the incident supported this finding. The combined static and thermal tilt had caused the runner to make contact with the thrust pads on the inner edge. While the two oiled surfaces may have survived light contact without damage, once material began to gall, the problem rapidly escalated until the resulting damage was great enough to halt the antenna motion.

To address the deductions of the investigation team, a number of upgrades were performed to reduce tilt, increase nominal lift, and improve monitoring of the bearing performance. New adjustable jacking struts were mounted around the perimeter of the thrust runner to mitigate the static deformation from the weight of the structure. The entire hydraulic system was reworked to increase the oil flow and improve monitoring. Finally, a network of eddy-current sensors was installed in the bearing to directly monitor the ride height and tilt of the runner.

The upgrades proved successful, and control system testing resumed with a number of new interlocks and monitoring points added to the control system software. As of this writing, the bearing has been operating without further problems for more than a year, increasing the team's confidence that the root causes have been addressed.

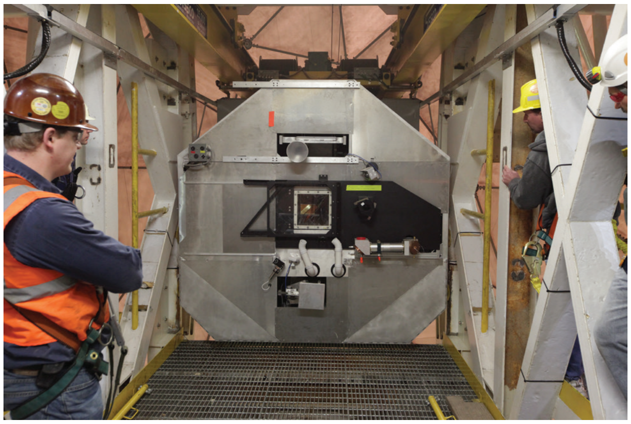

FIGURE 55. The front of the Octagon enters the tunnel through the transition structure as it is being installed for the first time on the new antenna.

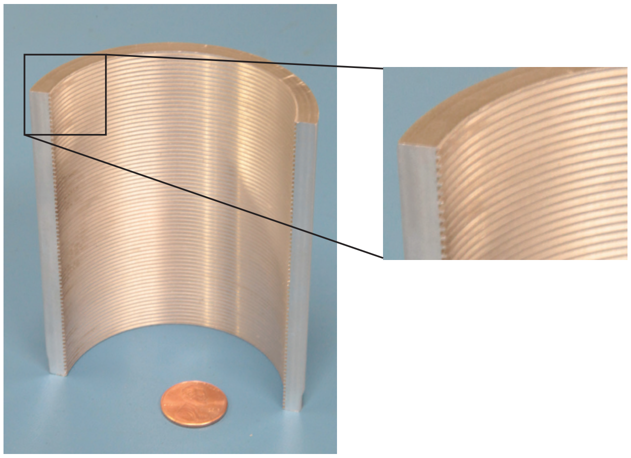

FIGURE 56. A sectioned piece of W-band waveguide shows the discrete corrugations on the interior surface.

RF Box Installation, January 2012

The final component of the new HUSIR antenna was integrated when the modified RF box with the new Octagon structure attached was lifted into place by the RFBIS hoist system (Figure 55). Once the RF box was in place, the final connections (power, signal, RF, water, air, helium) were established and tested, and the final sections of the W-band waveguide were installed.

Unlike the existing X-band radar system, which generates its 260 kW (peak) pulses in vacuum tubes inside

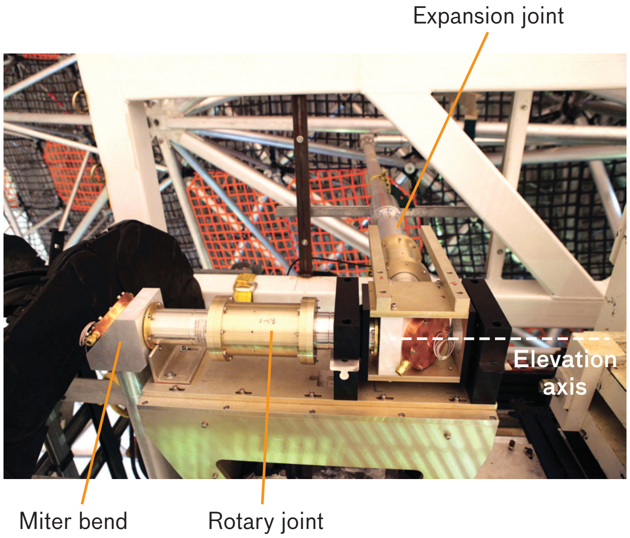

FIGURE 57. The elevation axis has a rotary joint to permit rotation and an expansion joint to account for the sag of the backstructure as it rotates to zenith.

the RF box, the ~1 kW (peak) W-band transmitter is located in an adjacent building, and signals are transmitted via a 300-foot run of overmoded (HE_{11}) circular waveguide. The W-band waveguide is an aluminum tube with a 2.5-inch inside diameter and a series of precisely spaced annular grooves cut into the inside wall (Figure 56). To minimize loss along the waveguide run, the 7-foot-long sections of waveguide were precisely aligned to avoid angular deviations greater than 0.05° or discontinuities at the junction between sections. To account for thermal expansion between the aluminum waveguide and the steel or concrete sections of the antenna, the design incorporates several expansion joints (Figure 57).

The waveguide passes through the Haystack office building and into the base of the antenna, where it intersects the azimuth axis. It follows the azimuth axis into the yoke before turning to follow the left yoke arm to the elevation axis. A rotary joint in each axis permits the circularly polarized signal to accommodate antenna motion. A final waveguide run through the backstructure enters the RF box, where the signal is converted to linear polarization prior to entering the duplexer mounted in the Octagon. Here, the transmit signal is sent out the aperture via the frequency-selective surface, and the return signal is routed into a cryogenically cooled receiver mounted below the duplexer.

In early spring 2012, the antenna surface underwent a final alignment that was performed with the newly developed holography technique. The holography measurements were able to gather high-quality data in a short time frame, enabling the workers in the nets to bring the surface error under 80 μm (in favorable thermal conditions). The details of this activity are contained in the accompanying article "Optimizing the HUSIR Antenna Surface."

First Light, May 2013

The completed W-band radar had its first light in May 2013 and its official return to service in February 2014 after a careful checkout period. The images produced by HUSIR have met and exceeded the expectations of the project and will provide a new level of space situational awareness for the country at a time when satellites are becoming increasingly smaller and more critical to our everyday lives.

Acknowledgments

The author would like to thank Todd Mower, Keith Doyle, John Ingwersen, Michael Glynn, Joe Usoff, James Eshbaugh, Bill Brown, and Mark Czerwinski for reviewing and/or contributing to this article. He would also like to thank Joe Antebi, Frank Kan, Dan Valentine, and Andrew Sarawit of Simpson Gumpertz & Heger for consulting on questions related to the design of the antenna and for submitting the accompanying appendix. ■

REFERENCES

1. H.G. Weiss, W.R. Fanning, F.A. Folino, and R.A. Muldoon, "Design of the Haystack Antenna and Radome," *Structures Technology for Large Radio and Radar Telescope Systems.* Cambridge: MIT Press, 1969.
2. K.B. Doyle, M. Brenner, J. Antebi, F.W. Kan, D.P. Valentine, and A.T. Sarawit, "RF-Mechanical Performance for the Haystack Radio Telescope," *Proceedings of SPIE,* vol. 8125, pp. 81250A-1–81250A-9.

ABOUT THE AUTHOR

Nikolas T. Waggener is a member of the technical staff in the Mechanical Engineering Group at Lincoln Laboratory. He has been involved with the HUSIR upgrade since 2007 and was responsible for the waveguide installation, old backstructure removal, subframe installation, and hydrostatic bearing refurbishment. He received a bachelor's degree in mechanical engineering from Worcester Polytechnic Institute.

Appendix

HUSIR Structural Design, Optimization, and Predicted Performance

This feature was contributed by Joseph Antebi, Frank W. Kan, Daniel P. Valentine, and Andrew T. Sarawit of Simpson Gumpertz & Heger Inc., the engineering firm that worked with Lincoln Laboratory to build the HUSIR antenna structure. The article is based on material published in Valentine et al. [a].

For the HUSIR upgrade, the tower, hydrostatic azimuth bearing, azimuth main gear, and yoke structure used with the original antenna were retained with some modifications. However, the tops of the yoke arms were replaced. The HUSIR antenna system uses a removable RF box that houses a series of feeds for different bands that are offset at different locations in the Cassegrain focal plane.

Table A1 lists key design parameters for the new antenna system. The F/D ratio and the subreflector diameter and eccentricity were kept the same as in the original antenna system so that legacy receivers and feeds could be reused with the new antenna.

Structural Design

HUSIR's main reflector surface is partitioned into 104 aluminum subframes that hold 432 aluminum surface panels. The reflector subframes are mounted onto the all-aluminum backstructure, which consists of 16 radial rib assemblies with four interleaved quadrapod support outrigger trusses that are all mounted directly to the central aluminum torque ring at the center of the backstructure.

The aluminum torque ring is supported off the steel transition structure with eight pairs of steel/aluminum struts that produce a stiff mounting with respect to axial and lateral loads while permitting relatively unrestrained differential radial expansion between the two structures over the operating temperature range. The steel transition structure, which includes the drive arcs and the elevation bearings, is supported on the upgraded steel yoke. For both azimuth and elevation, new gearboxes with high-performance brushless motors replaced the hydraulic drives in the original system.

The major components of the new main reflector are

- Reflector panels on subframes
- Reflector backstructure and quadrapod
- Reflector support struts

Table A1. Key Antenna Design Parameters

SYMBOL	ITEM	VALUE	UNITS
F	Focal length of primary mirror	14.63	m
f	Distance from Cassegrain feed phase center to primary focal point	12.80	m
d	Subreflector diameter	2.84	m
D	Primary diameter	36.57	m
α	Cassegrain feed half angle	6.7	deg
ξ	Distance from primary focus to subreflector vertex	1.097	m
K	F/D	0.4	
φ_o	Main reflector half angle	64.0	deg
M	Cassegrain magnification factor	10.7	

- Transition structure (includes elevation bearing assemblies and elevation drive sector gears)
- RF box insertion and support system

Reflector Panels on Subframes

The 432 antenna reflector surface panels are aluminum grillage panels with 1.5 mm thick surface skins; the individual panels have a typical surface accuracy of 28 μm rms. During the fabrication process, each surface panel was measured at several hundred points using a laser tracker. Groups of four or five surface panels are installed onto each of the 104 aluminum subframe truss structures. The subframe truss structure with the panels attached forms a structurally stiff assembly. The subframe accepts 10 adjustable mounting points from each surface panel; these mounting points allow each surface panel to be aligned to the same desired parabolic surface, with all focal points aligned to very high accuracy.

During the final integration, each subframe was attached to the main backstructure rib trusses with a four-point mount adjusted to bring all subframes onto the same parabolic surface at the rigging angle of 25° elevation.

Main Reflector Backstructure

The design of the main reflector backstructure, shown in Figure A1, was iterated to achieve an optimal stiffness-to-weight ratio and to keep the anticipated thermal and gravitational deformations small enough for operations at 96 GHz with high aperture efficiency.

The backstructure's 16 radial rib assemblies cantilever from a central toroidal torque ring mounted onto the steel transition structure. The aluminum backstructure is connected to the steel transition structure by 16 support struts. Each radial rib assembly consists of one long and one short rib, with each rib having two top chords and one bottom chord; the nodes of the top chords are the support points for the subframes. The ribs are interconnected by hoop and diagonal members.

This backstructure configuration provides stiff support points for the subframes while minimizing the number of members and nodes and, hence, the backstructures's weight. The aluminum backstructure is fully welded with no mechanical fasteners except at the preloaded tension rods forming the outer hoop truss and the preloaded connection at the aluminum-to-steel interface.

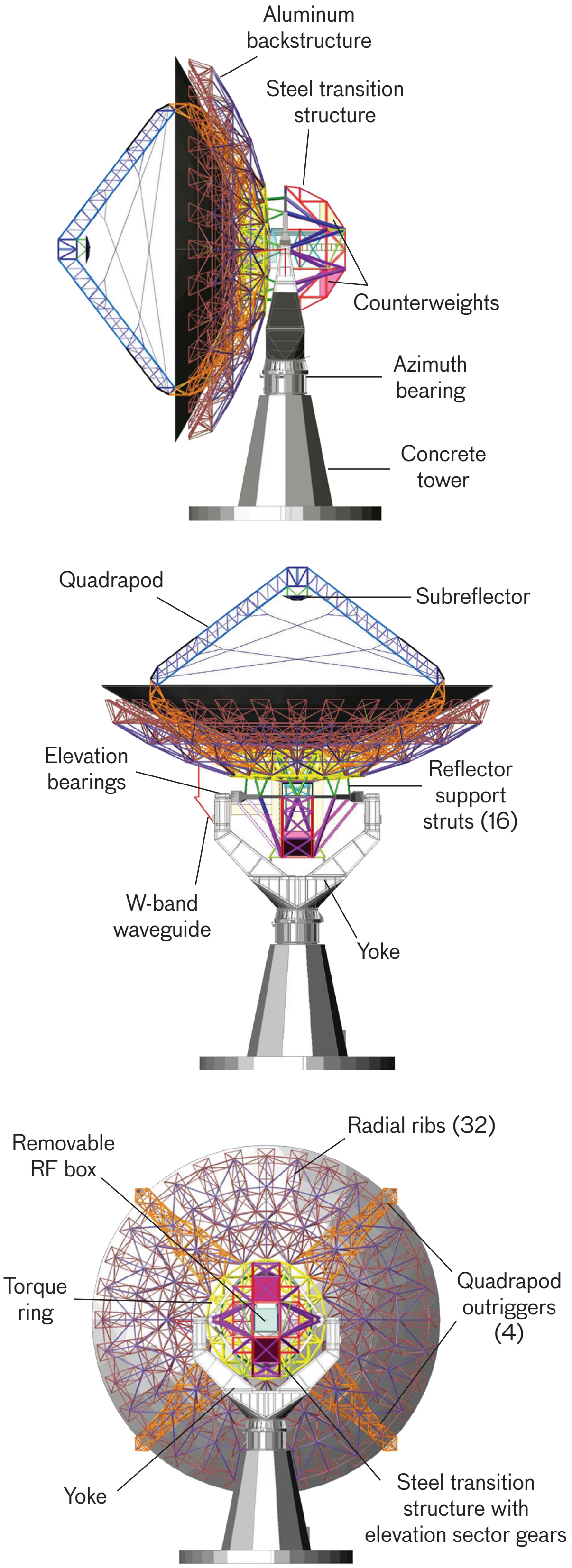

FIGURE A1. Face-side, face-up, and rear views of HUSIR.

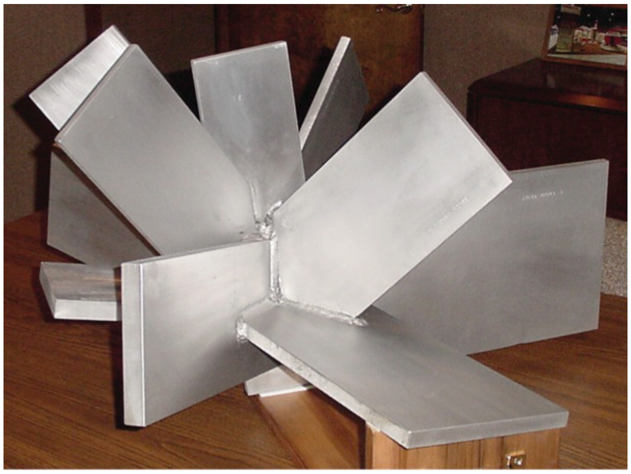

FIGURE A2. Typical backstructure node formed from aluminum plates welded together in a complex fixture.

FIGURE A3. Torque ring assembly fixture.

FIGURE A4. Fixturing of backstructure rib tubing to nodes prior to welding operations.

The radial ribs and torque ring of the aluminum backstructure were designed as space trusses. The nodes, formed by a series of aluminum plates welded together, are interconnected by aluminum tubes whose ends are slit and welded to the plates that form the nodes. The backstructure nodes consist of up to 15 intersecting plates welded together as subassemblies using precision jigs in a specific three-dimensional (3D) orientation. A typical node is shown in Figure A2. The nodes were welded with great care to achieve the precision necessary for proper fitting of the aluminum tubes placed between them during the 3D assembly of the backstructure. The backstructure and torque ring sections were fabricated using several precision assembly fixtures similar to the one shown in Figure A3. The backstructure rib assembly fixtures were precision aligned by laser trackers so that each node of the backstructure rib can be precisely located in 3D space.

Once the prefabricated nodes were positioned on the assembly fixture, the aluminum tubes were placed between the nodes and held with a series of clamps until welded in place (Figure A4). Welding was not done until the entire rib assembly was dry fitted. The welding was sequenced to minimize the development of constraint forces and the distortion upon the assembly's release from the jig.

The 16 aluminum rib assemblies and the central aluminum torque ring were built as subassemblies and transported to the final assembly building at the Haystack site. A completed rib assembly, which is about 12 meters long, is shown in Figure A5.

The quadrapod, which supports the subreflector, is itself supported beyond the perimeter of the reflector by outrigger trusses that cantilever from the torque ring. The outrigger trusses are interwoven with the 45° ribs (Figure A6) and therefore are independent from the radial ribs that support the main reflector subframes; this arrangement dramatically reduces common deformations caused by the interaction between the subreflector supports and the primary reflector. In addition, positioning the outrigger trusses beyond the perimeter of the reflector minimizes the RF blockage by eliminating the fan-shaped shadows that would extend outward from the base of the quadrapod legs if they were within the spherical wave-blockage region associated with the aperture.

To account for the difference between the coefficients of thermal expansion of the aluminum backstructure and the steel transition structure, the aluminum torque

FIGURE A5. Completed radial rib assembly.

ring at the center of the backstructure is supported by 16 reflector support struts, which allow radial expansion of the torque ring without introducing significant restraint forces. These reflector struts are part aluminum and part steel, with a preloaded bolted connection at the steel/aluminum interface, as shown in Figure A7. Stainless steel spacers are used between the aluminum and steel sections to preclude galvanic corrosion.

Transition Structure

The transition structure includes the elevation main gears, elevation bearings, counterweights, buffer stop contact pads, and the RF box insertion system. The two elevation main gears, located symmetrically to either side of the central RF box, have a 6.1 m pitch radius, an increase from the 1.8 m radius gears used in the original antenna. These larger main gears increase the drive stiffness to allow for greater velocity and acceleration, and raise the natural frequency of the system. The elevation counterweights are mounted to the rear side of the transition structure between the main gears in two groups located above and below the RF box insertion tunnel.

The 16 reflector support struts are mounted in pairs at eight points on the front face of the transition structure, as shown in Figure A8; these eight points are supported by struts to the rear of the transition structure and thence the loads are carried forward to the elevation bearings. With this configuration, the stiffness of the load paths from the eight points on the front face to the elevation bearings can be equalized.

The elevation bearings are spherical roller bearings mounted in the transition structure and supported by stub shafts cantilevering from the tops of the yoke arms. In this configuration, with the spherical bearings in the elevation structure, the bearings act as “pin supports” for the transition structure, having little or no restraint with respect to moments, but having high stiffness with respect to radial and axial loads. Once the bearings are axially preloaded, the vertical loads on the stub shafts are nearly constant as the antenna moves in elevation, precluding reaction forces being transferred into the transition structure. Such reaction forces, if present, would have a deleterious impact on backstructure deflections as a function of elevation angle.

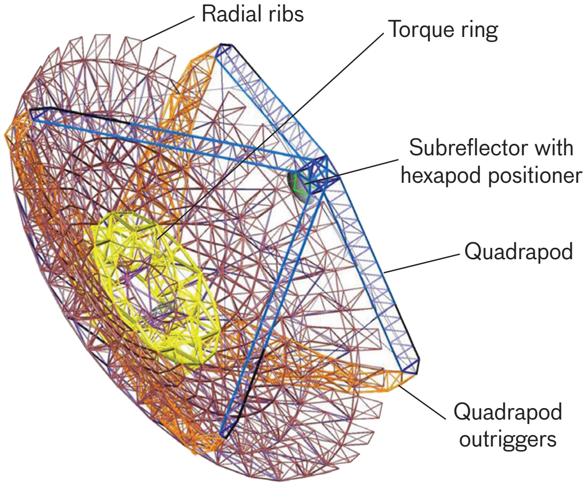

FIGURE A6. Aluminum backstructure with subreflector, quadrapod, and outriggers.

The steel transition structure subassemblies were assembled, aligned, and welded on the ground at the site prior to their being lifted into position on the yoke. The support of the stub shafts at the top of the yoke included provisions for adjustments so that, when the entire antenna was assembled, the elevation axis was aligned to be horizontal and to intersect the azimuth axis. Then an axial load was applied between the yoke arms to preload the spherical bearings such that there is no load reversal in the bearings and the antenna's behavior is predictable and repeatable.

RF Box Insertion System

With the antenna at horizon pointing, the RF box was hoisted from the ground into the transition structure by using the newly designed RF box insertion system (RFBIS), shown in both the retracted position and in the installed operational position in Figure A9. The RFBIS is similar to the hoist system used in the original antenna but has a higher capacity; it allows the RF box to be rolled forward into position at the Cassegrain focus, where it is locked down into a support structure attached to the torque ring.

Particular attention was given to preserving the stiffness and precise location of the RF box structural mounting features so that the antenna has excellent and repeatable pointing and tracking characteristics in the shorter millimeter-wavelength bands from 80 to 230 GHz.

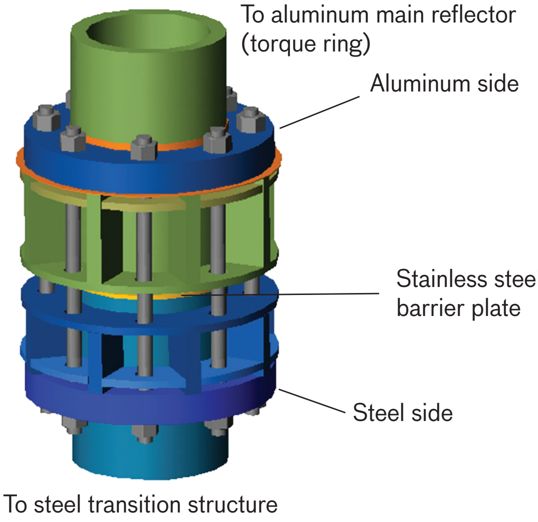

FIGURE A7. Preloaded bolted connection at steel-to-aluminum interface in each reflector support strut.

Structural Design Optimization

Starting with an initial configuration, the design of the subframes and backstructure members was optimized to select nominal member sizes for minimum weight, subject to constraints on surface rms resulting from gravity and minimum natural frequency.

A comprehensive structural model of the entire antenna system was developed and optimized using MSC Software's NASTRAN (originally called NASA Structure Analysis) finite element analysis program with the Jet Propulsion Laboratory's Antenna Optimization (JPL-ANTOPT) software [b]. This model included the compliance of the existing tower and yoke, as well as the new gear trains, transition structure, main reflector backstructure, and weights of the subframes and surface panels. On the basis of the optimized model, we selected

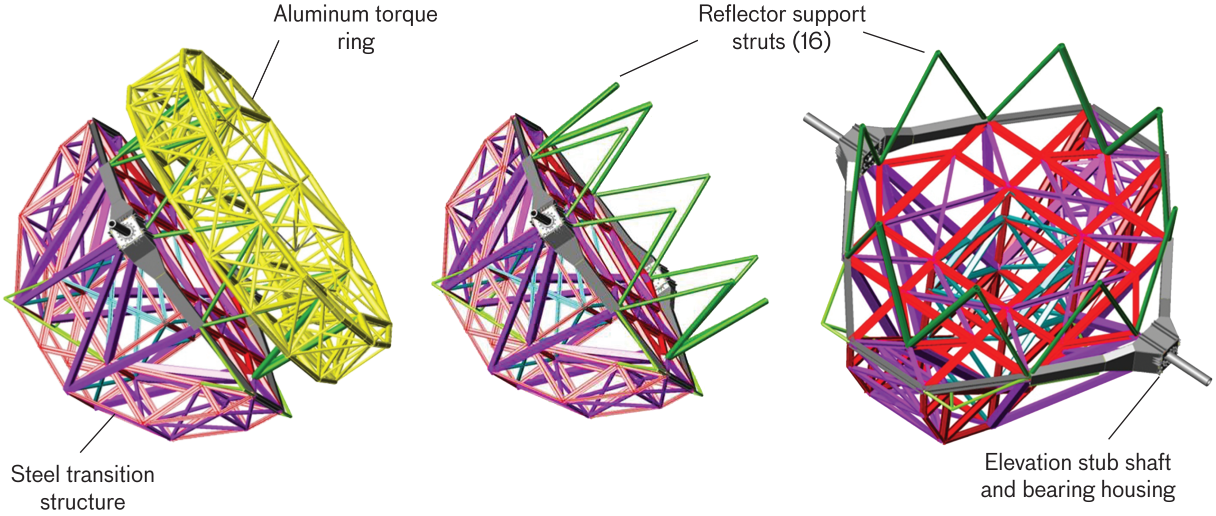

FIGURE A8. Steel transition structure and connection to aluminum torque ring on main reflector.

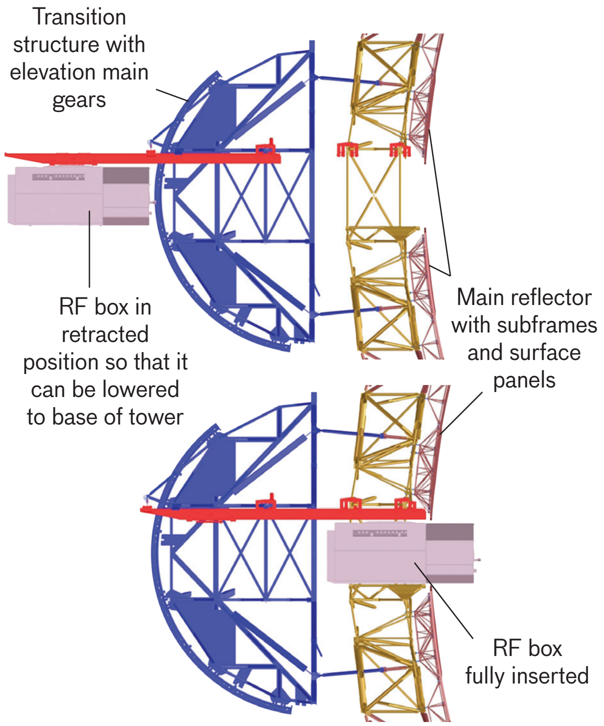

FIGURE A9. The RF box insertion system shown in the retracted (top) and operational configuration (bottom).

the actual backstructure members, taking into account availability and choosing wall thicknesses so as to reduce the thermal distortions caused by differences in thermal lag between adjacent members.

The connections at the nodes then underwent detailed finite element analyses and several design iterations to ensure that the combined stiffness of a member and its end connections would match the stiffness of the overall member as required by the structural optimization.

Optimization of Connections

After the backstructure was optimized to meet surface rms requirements, random-error analyses were performed to determine the sensitivity of the surface rms to variations in the effective stiffnesses of members. These analyses were performed by using a random-number generator to introduce uniformly distributed stiffness errors to the backstructure members. These imposed errors were constrained to remain within a given stiffness tolerance. The variations under consideration were the combined effects of the stiffness of the connections plus the effects of tolerances on cross sections and on fabrication. The surface displacements from each analysis were used to compute surface rms values. For all the surface rms calculations, we used the optimal subreflector position adjustments predicted on the basis of the nominal design. This approach is conservative since in practice the subreflector adjustments would be based on tests to maximize gain.

The sensitivity analyses were run with stiffness tolerances set at ±5% and at ±10%. At ±5% tolerance on stiffness, the surface rms increased by 1.1% and 1.4% for gravity at zenith and horizon pointing, respectively. At ±10% tolerance on stiffness, the surface rms increased by 3.4% and 3.7%, respectively. The increase in surface rms with tolerances on effective stiffnesses emphasized the need to design the connections to closely match the required effective stiffness of the overall member so as to have some margin for the other causes of variations in stiffness, which are hard to control.

Joint Configuration

The optimized backstructure required a variety of tubing cross sections. Using several of these cross sections to represent the range of tubing diameters and wall thicknesses, we undertook a parametric study to determine the effective stiffness of tube/gusset configurations. In addition to the gusset width and thickness, the depth of the slot and associated weld length are parameters that can be used to adjust the stiffness of a connection. The complexities of typical connections are illustrated in Figures A10 and A11.

Given the complexity of the backstructure trusswork, which is composed of curved space trusses positioned radially around a central axis, multiple members in many instances share a single gusset plate. Therefore, a given gusset plate must accommodate tubing members with appreciably different diameters and wall thicknesses, with the wall thickness variations providing conflicting values for selecting a single gusset plate thickness. In some cases, a thin gusset had to be welded onto the edge of a thicker one, thereby increasing the effective stiffness of the smaller member.

Finite Element Model of Connection

To determine the effective stiffnesses of the members coming into a given connection, a detailed finite element model was constructed with a mesh fine enough to capture the localized behavior. Specifically, the model had to capture (1) the shear deformation in the tubing wall and in the gusset plate as the forces are transferred

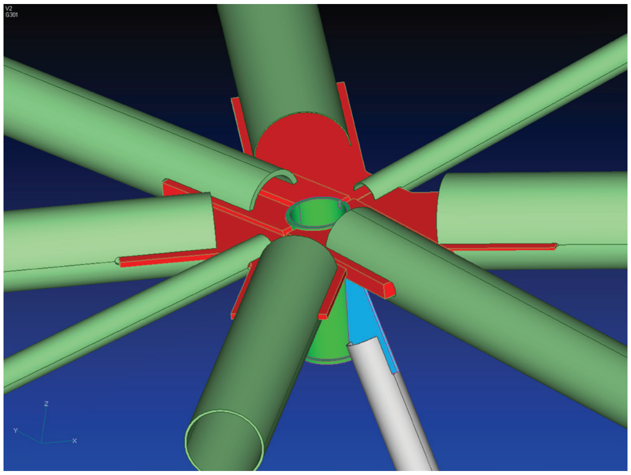

FIGURE A10. Top surface connection of space truss with 9 members framing into it.

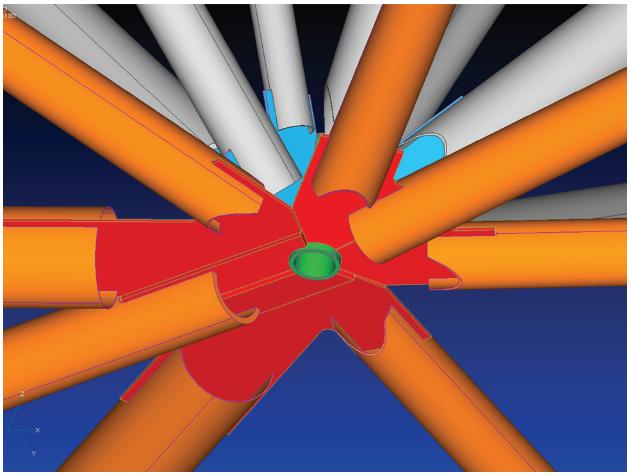

FIGURE A11. Underside view of a bottom surface connection of a space truss with 16 members. The figure illustrates the variation of wall thicknesses in the members and the way gusset plates of various thicknesses were joined together to form the connection. Note that the chamfers on the ends of some members were used for clearance between members and not for stiffness adjustment.

through the welds, and (2) the out-of-plane distortions of the plates and tubing wall. The level of detail required is illustrated in Figure A12. For every node configuration, the entire connection was modeled along with portions of the tubing members.

The model was analyzed with a series of load cases; each case had an axial load applied to the far end of one of the members. The non-loaded members were restrained at their far ends, taking into account the gusset plate orientation at that particular end. The effective stiffness of each member in turn was determined on the basis of the axial displacement of the mid-length of the tube with respect to the displacement of the working point of the connection. The effective stiffnesses thus obtained were then compared to the nominal stiffnesses of the members spanning between working points. Using these results, we modified the connection to increase or decrease the stiffness of each member as appropriate, and we then analyzed the adjusted model and repeated the process until satisfactory behavior was obtained.

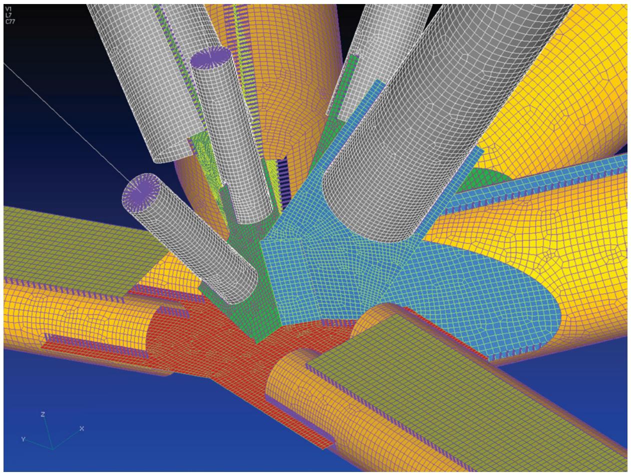

FIGURE A12. Illustration of a finite element model of a connection with 11 members framing into it.

During the initial structural optimization process, the weights of the connections were unknown. To compensate for this, each connection was initially assumed to weigh 15% of the weight of the members spanning into it. This assumption was built into the models by increasing the density of the materials by 15%. But, in conjunction with designing the connections to achieve desired stiffness values, finalizing the configuration of the connections permitted an accurate assessment of the connection weight. For the final analysis model of the structure, the actual weights computed for each connection were used in lieu of the 15% density increase. The results showed that the 15% allowance was reasonable as an overall average. However, for connections that had very lightweight members, the connections corresponded to almost 40% of the member weights; for connections that had numerous heavy members, the values were as low as 3%.

Similar finite element analyses were conducted on the subframes and the surface panels to determine optimum sizes for all structural members.

Table A2. Surface Error Budget

CONTRIBUTION FACTOR	BUDGETED RMS (μm)
Manufacturing	
Panel	30
Gravity deformation	
Panel	12
Subframe	See below
Backstructure	See below
Thermal—stable condition	
Panel	10
Subframe	20
Backstructure	70
Alignment	
Panel	30
Subframe	35
Combined—stable condition at 25° rigging angle	87
Backstructure gravity	
Face up	176
Face down	171
Subframe gravity	
From elevation= 25° to 0°	5
From elevation= 25° to 90°	24

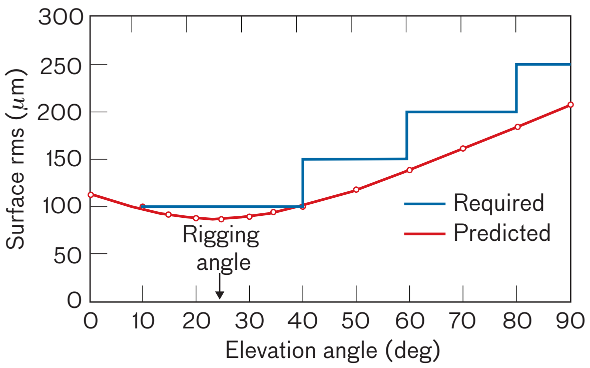

FIGURE A13. Predicted surface rms error when bias-rigged at 25° elevation.

The design was then evaluated over the range of elevation angles and expected temperature distributions to assess the overall performance of the complete system for use up to 230 GHz, with good dynamic tracking characteristics and with a predicted surface accuracy within the bounds of the operational requirements.

Predicted Performance

Table A2 shows the error budget for the factors that contribute to the overall rms surface error for the new antenna system. The panels and subframe contributions have been confirmed by measurement, and the other factors have been estimated from the NASTRAN model.

It is possible to estimate the overall rms accuracy expected for this antenna system at different elevation angles (E) by using the well-known backstructure gravity deflection relation

$$\mathrm{rms}(E)=\Big[FU^2\big(\sin(E)-\sin(E_{\mathrm{rig}})\big)^2 + FS^2\big(\cos(E)-\cos(E_{\mathrm{rig}})\big)^2\Big]^{1/2} \qquad (1)$$

where FU and FS are the face-up and face-side surface rms determined from the model and E_{rig} is the elevation rigging angle.

The measured and calculated values in Table A2 were used with Equation (1) to calculate the combined surface rms at all elevation angles between the horizon and zenith with the antenna bias-rigged for 25°. The antenna was rigged at 25° to achieve optimal performance at elevation angles between 10°and 40°, the range at which most observations are conducted at the Haystack site. Results of this analysis, shown in Figure A13, indicate that, in the operational region from 10° to 40° elevation angle, the antenna will provide 87 to 100 μm rms surface accuracy.

REFERENCES

a. D.P. Valentine, F.W. Kan, and J. Antebi, "Design Optimization of Connections in Large Radio Telescopes," *Optomechanical Technologies for Astronomy, Proceedings of SPIE*, vol. 6273, 2006, pp. 627313-1–627313-8.

b. D.M. Strain, "JPL-ANTOPT Antenna Structure Optimization Program," *Telecommunications & Data Acquisition Progress Report* 42-119, Pasadena, Calif.: Jet Propulsion Lab., Caltech, Nov. 1994, pp. 282–292.